J. Fluid Mech. (2014), *vol.* 756, *pp.* 1058–1091. © Cambridge University Press 2014. This is a work of the US Government and is not subject to copyright protection in the United States.
doi:10.1017/jfm.2014.475

Pressure fluctuations beneath instability wavepackets and turbulent spots in a hypersonic boundary layer

Katya M. Casper[1,2,†], Steven J. Beresh[1] and Steven P. Schneider[2]

[1]Sandia National Laboratories, Albuquerque, NM 87185, USA

[2]Department of Aeronautics and Astronautics, Purdue University, West Lafayette, IN 47907, USA

(Received 20 September 2013; revised 15 May 2014; accepted 12 August 2014; first published online 9 September 2014)

To investigate the pressure-fluctuation field beneath turbulent spots in a hypersonic boundary layer, a study was conducted on the nozzle wall of the Boeing/AFOSR Mach-6 Quiet Tunnel. Controlled disturbances were created by pulsed-glow perturbations based on the electrical breakdown of air. Under quiet-flow conditions, the nozzle-wall boundary layer remains laminar and grows very thick over the long nozzle length. This allows the development of large disturbances that can be well-resolved with high-frequency pressure transducers. A disturbance first grows into a second-mode instability wavepacket that is concentrated near its own centreline. Weaker disturbances are seen spreading from the centre. The waves grow and become nonlinear before breaking down to turbulence. The breakdown begins in the core of the packets where the wave amplitudes are largest. Second-mode waves are still evident in front of and behind the breakdown point and can be seen propagating in the spanwise direction. The turbulent core grows downstream, resulting in a spot with a classical arrowhead shape. Behind the spot, a low-pressure calmed region develops. However, the spot is not merely a localized patch of turbulence; instability waves remain an integral part. Limited measurements of naturally occurring disturbances show many similar characteristics. From the controlled disturbance measurements, the convection velocity, spanwise spreading angle, and typical pressure-fluctuation field were obtained.

Key words: high-speed flow, instability, transition to turbulence

1. Introduction

1.1. *Motivation*

Hypersonic vehicles are subjected to high levels of fluctuating pressures. These intense fluctuations cause vibration of internal components and can lead to structural problems. There is a need to predict the magnitude, location, and spatial extent of the pressure fluctuations to better design hypersonic flight vehicles. Current vehicle designs often use overly conservative estimates of the fluctuations which

† Email address for correspondence: kmcaspe@sandia.gov

https://doi.org/10.1017/jfm.2014.475 Published online by Cambridge University Press

lead to heavier vehicles, degraded flight performance, and excessively cautious predictions of the effects on internal components. Some correlations exist for the magnitude of transitional and turbulent pressure fluctuations, but these were derived primarily using either incompressible data or conventional (noisy flow) hypersonic wind-tunnel tests (e.g. Houbolt 1966). Such modelling efforts have not led to sufficient physical understanding of the transitional pressure fluctuations or adequate predictive capabilities. Incompressible data do not include high-speed phenomena such as second-mode instability waves, which will be shown to be an integral component of the transitional disturbances in a hypersonic boundary layer. Also, most data are contaminated by noise radiated from the tunnel walls, which can mask the transitional physics.

During boundary-layer transition, the heating rates and pressure fluctuations are higher than for a fully turbulent boundary layer (e.g. Pate & Brown 1969). These high pressure fluctuations result from repeated intermittent spatial–temporal switching between laminar and turbulent regions, creating a broad spectrum of disturbances. Unfortunately, natural transition typically occurs in flight over a large portion of the vehicle (Johnson *et al.* 1972), making transitional fluctuations of primary interest for this work.

A more physically based approach to modelling these transitional pressure fluctuations can be developed by using an intermittency model of transition. This semi-empirical model is based on the growth and propagation of turbulent spots in the transitional boundary layer (Dhawan & Narasimha 1958; Narasimha 1985). There are three main parameters that describe the intermittency model of transition: the transition onset location, the spot formation rate per unit span, and a spot growth parameter. Knowing these values, the transition length can be computed. This type of transition model allows the computation of flow properties throughout transition (Vinod 2007; Park & Lauchle 2009; Zharov, Htun & Khlopkov 2009). By incorporating the pressure fluctuations associated with wavepackets and turbulent spots, the models can be extended to calculate transitional pressure fluctuations from fundamental physics. This type of model has already been developed for incompressible flow on a flat plate (Park & Lauchle 2009).

To use this model for a flight environment, the transition onset location must be known. This can be obtained either from existing flight data or by using stability computations and the e^N method to estimate transition onset. The formation rate of the spots must also be known. This parameter might be inferred from flight data for the transition length. However, there are limitations to flight tests which often contain sparse instrumentation. The spot growth parameters must also be determined, as must the distribution of pressure fluctuations within the spots.

These last pieces of the model are the focus of the present work. To the authors' knowledge, no measurements of the internal structure of the pressure field under a hypersonic turbulent spot have been made prior to this work. Recent direct numerical simulation (DNS) efforts have also studied wavepackets and developing turbulent spots in hypersonic boundary layers (Krishnan & Sandham 2006*a*; Joksch & Kleiser 2008; Sivasubramanian & Fasel 2010*a*,*b*, 2011; Redford, Sandham & Roberts 2012). These computations provide valuable information about the spot structure and growth parameters, but they have not yet studied the evolution of the associated pressure-fluctuation field in depth. Experimental data are necessary to validate these transition simulations. Together, the computations and experiments can be used to develop an analogue to Park & Lauchle (2009)'s incompressible model for pressure fluctuations in high-speed flow on a more complex geometry. Of course, there are still

https://doi.org/10.1017/jfm.2014.475 Published online by Cambridge University Press

limitations and assumptions that are involved in developing these models. The present experimental work can help determine what model assumptions will sufficiently capture relevant physics, especially at higher Mach numbers where experimental data are lacking.

To make detailed studies of the boundary-layer disturbances, measurements of instability-wavepacket and turbulent-spot pressure fluctuations were made on the nozzle wall of the Boeing/AFOSR Mach-6 Quiet Tunnel (BAM6QT). More detail about the present work can be found in several conference papers and a dissertation (Casper, Beresh & Schneider 2011*a*,*b*, 2012; Casper 2012). The BAM6QT can be operated under aerodynamically quiet-flow conditions in which laminar boundary layers are maintained on the wall of the wind tunnel. Laminar flow avoids the generation of pressure-fluctuation 'noise' usually radiated from the turbulent walls of conventional tunnels (Schneider 2008). Because the boundary layer grows over the entire nozzle length, it is of the order of 10 mm thick in the test section (Wheaton 2009). As a result, turbulent spots can grow much larger along the nozzle in comparison to a typical 1 m long model in the tunnel. The smaller spots on the nozzle wall can be many centimetres long, with the largest spots of the order of a metre long. These larger spots give better relative resolution with the available pressure sensors, in comparison with measurements on a typical model.

Naturally occurring wavepackets and turbulent spots on the tunnel wall were studied under quiet-flow conditions. However, the initial spanwise location of these disturbances relative to the sensors is unknown, and the disturbances cannot be repeated. To study controlled disturbances, a pulsed-glow perturber was used to create repeatable wavepackets that would break down into turbulent spots. Measurements were made along the disturbance centrelines and in the spanwise direction to characterize the associated pressure fluctuations. The measurements were then used to estimate several spot growth parameters that can be included in engineering models for the transitional pressure fluctuations.

1.2. *Previous work*

1.2.1. *Internal structure of turbulent spots*

The internal structure of turbulent spots has been extensively studied, mostly in incompressible flow. The typical shape of a turbulent spot (e.g. Schubauer & Klebanoff 1955; Krishnan & Sandham 2006*a*) is shown in figure 1. The spots have a characteristic downstream-pointing arrowhead shape that can be defined by a lateral spreading half-angle as well as a front half-angle (Schubauer & Klebanoff 1955). At the front of the spot, there is an overhang region where the turbulence within the spot is lifted from the wall. There are also overhang regions on the sides of the spot. The overhang region at the front of the spot is composed of older turbulence, while newer turbulence is generated at the tail of the spots (Singer 1996). Following the passage of a turbulent spot, there is a calmed region, marked by a more full velocity profile and lower pressures than the undisturbed boundary layer (Schubauer & Klebanoff 1955). This region is more stable than the natural boundary layer because of the fuller velocity profile.

Wavepackets are often observed in the calmed region behind the spots (Wygnanski, Zilberman & Haritonidis 1982; Chambers & Thomas 1983; Glezer, Katz & Wygnanski 1989). These packets usually have the largest amplitude at the wing tips of the spot planform. Glezer *et al.* (1989) observed that the wavepackets would break down to turbulence only when the surrounding boundary layer was unstable. These new patches

https://doi.org/10.1017/jfm.2014.475 Published online by Cambridge University Press

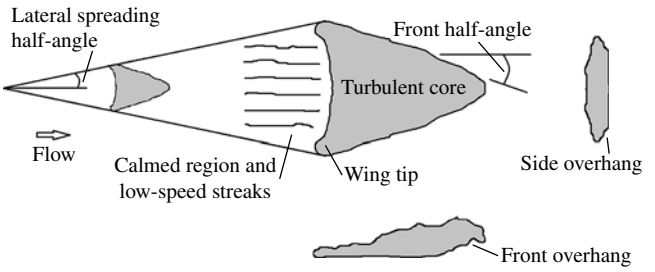


FIGURE 1. Sketch of a turbulent spot.

of turbulence would later merge with the upstream spot. In stable boundary layers, the packets would not break down and sometimes decayed.

Recent DNS studies have investigated the spot structure at hypersonic Mach numbers (Krishnan & Sandham 2006*b*; Joksch & Kleiser 2008; Sivasubramanian & Fasel 2010*a*; Redford *et al.* 2012). At hypersonic conditions, boundary-layer instabilities become important. One of the dominant instabilities at hypersonic speeds is the second-mode instability, or the second Mack mode (Mack 1984). The second-mode waves act like trapped acoustic waves that reflect between the wall and near the boundary-layer edge. As a result, the frequency of the waves is inversely proportional to the boundary-layer thickness. The most amplified waves propagate with the wavefronts perpendicular to the flow direction. Initially, the unstable waves are linear. Prior to transition, the waves grow, become nonlinear, and break down to turbulence. DNS computations by Krishnan & Sandham (2006*b*) and Redford *et al.* (2012) found that turbulent spots at Mach 6 have spanwise coherent structures related to the Mack modes under the front overhang region of the spots. These structures are not seen at the lower Mach numbers (2–4) that were also computed. DNS results by Sivasubramanian & Fasel (2010*a*) also showed that second-mode waves were an integral part of the disturbances as they break down into turbulent spots.

1.2.2. *Spot growth*

Spot growth is an important parameter in turbulent spot models. The spot growth is different in the wall-normal, streamwise, and spanwise directions and can be attributed to different physical phenomena (Corrsin & Kistler 1955; Wygnanski, Sokolov & Friedman 1976; Cantwell, Coles & Dimotakis 1978; Gad-el Hak, Blackwelder & Riley 1981; Wygnanski *et al.* 1982; Riley & Gad-el Hak 1984; Gutmark & Blackwelder 1987; Sankaran & Antonia 1988; Sankaran, Sokolov & Antonia 1988; Glezer *et al.* 1989; Katz, Seifert & Wygnanski 1990; Haidari & Smith 1994; Seifert, Zilberman & Wygnanski 1994; Seifert & Wygnanski 1995; Singer 1996; Krishnan & Sandham 2006*a*,*b*). In the wall-normal direction, the growth of the spots is governed by classical entrainment. In the streamwise direction, growth has been attributed to the generation of new turbulence which occurs primarily in the tail of the spot and destabilization of the laminar flow under the overhang region of the spot. In the lateral direction, the spot grows by destabilizing the surrounding laminar boundary layer. The stability of the surrounding boundary layer as well as pressure gradients can affect the growth rate of the turbulent spots.

The streamwise growth can be quantified by measuring the difference in the convection velocity of the spot front (U_{le}) and tail (U_{te}). High-speed experiments give a range of U_{le}/U_e from 0.81 to 0.94 and U_{te}/U_e from 0.41 to 0.63, where U_e

https://doi.org/10.1017/jfm.2014.475 Published online by Cambridge University Press

is the boundary layer edge velocity (Zanchetta 1996; Mee 2002; Fiala *et al.* 2006). DNS computations on a flat plate at Mach 6 gave a leading-edge convection speed of $0.89U_e$ and a trailing-edge convection speed of $0.68U_e$ (Krishnan & Sandham 2006*a*). Other DNS computations of turbulent spots with hot and cold walls at Mach 3 and 6 found front convection velocities between $0.85U_e$ and $1.0U_e$ and rear convection velocities between $0.60U_e$ and $0.75U_e$ (Redford *et al.* 2012).

Lateral growth is characterized by a lateral spreading half-angle. Fischer (1972) collected experimental data for this angle across a broad range of Mach numbers. These values were determined from experiments behind roughness elements and in turbulent spots. Typically, low-frequency techniques such as oil-flow visualization and ablation patterns were used. The lateral spreading angle decreases from approximately 9° to 11° for incompressible flow down to 2°–4° at hypersonic edge Mach numbers. The upper limit of experimental data collected by Fischer is at an edge Mach number of 8. For data near a free-stream number of Mach 6, recent DNS computations of the spreading angle in compressible boundary layers support Fischer's results (Krishnan & Sandham 2006*a*; Sivasubramanian & Fasel 2010*a*; Redford *et al.* 2012). However, some high-speed experiments show larger values up to 12° (James 1958; Fiala *et al.* 2006). It is difficult to compare these various experimental results and DNS because of the different criteria used to define the edges of the spots in each study.

1.3. *Wall pressure field*

In order to develop a spot-based model of pressure fluctuations, the wall pressure field associated with a turbulent spot must be known. Prior to recent experiments (Casper *et al.* 2011*a*,*b*, 2012; Casper 2012), the internal structure of the pressure field underneath turbulent spots has only been measured experimentally in incompressible flow (Cantwell *et al.* 1978; Savas 1979; Mautner & Van Atta 1982; Mautner 1983, 1988; Johansson, Her & Haritonidus 1987). These low-speed measurements have primarily studied ensemble-averaged pressure traces. There is very little discussion of the higher-frequency fluctuations within the spot and little data characterizing them. There is also no mention of instability waves being an integral part of the disturbances.

Compressible turbulent spots are of interest for modelling transitional pressure fluctuations on hypersonic re-entry vehicles. The majority of experiments studying turbulent spots in hypersonic boundary layers have used thin-film heat-transfer gauges (Lagraff & Jones 1995; Mee & Goyne 1996; Zanchetta 1996; Fiala *et al.* 2006). Schlieren and shadowgraphy techniques have also been used to visualize the turbulent spots (James 1958; Wadhams *et al.* 2008). However, these results were not analysed in detail to study the structure or growth of the turbulent spots. Also, many of these experiments were conducted with a supersonic edge Mach number, where the second-mode instability would not be present.

Despite these experiments, to the authors' knowledge, no measurements have been made of the internal structure of the pressure field beneath turbulent spots in a compressible, hypersonic boundary layer. There are measurements of pressure fluctuations beneath instability wavepackets leading to transition (e.g. Fujii 2006; Estorf *et al.* 2008; Casper 2009; Berridge 2010), but not beneath turbulent spots. Some DNS computations of turbulent spots in hypersonic boundary layers have also been completed (Krishnan & Sandham 2006*a*,*b*; Joksch & Kleiser 2008; Sivasubramanian & Fasel 2010*a*, 2011). Together, these experiments and DNS studies can be used to understand how this pressure-fluctuation field evolves as turbulent spots develop in order to correctly model the transitional pressure fluctuations.

https://doi.org/10.1017/jfm.2014.475 Published online by Cambridge University Press

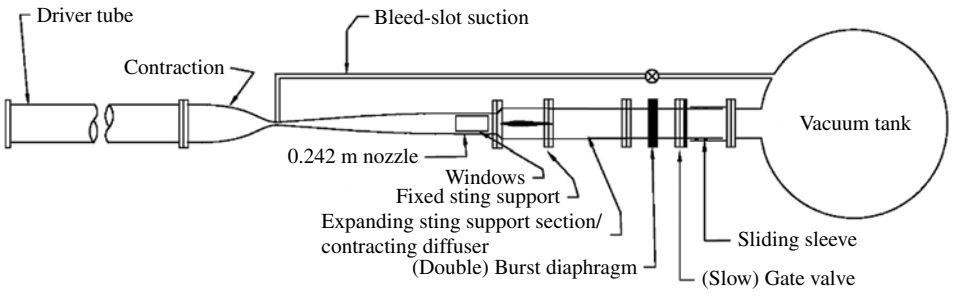


FIGURE 2. Schematic of the Boeing/AFOSR Mach-6 Quiet Tunnel.

2. Experimental methods and set-up

2.1. *Boeing/AFOSR Mach-6 Quiet Tunnel*

Measurements were made on the nozzle wall of the BAM6QT (figure 2). This tunnel is one of three hypersonic quiet tunnels in the world. The tunnel is a Ludwieg tube: a long pressurized tube with a converging–diverging nozzle on the end. The flow passes from the driver tube, through the test section, diffuser, and finally to the vacuum tank. Flow is initiated by bursting a double diaphragm that is located downstream of the diffuser. When the flow begins, an expansion wave travels upstream and then reflects between the upstream end of the driver tube and the contraction. The total pressure and temperature drop with each reflection cycle (every 200 ms). Run times of 3–5 s are typical under quiet-flow conditions. The tunnel uses air as the test gas and operates with an initial total pressure P_0 of 34–2070 kPa and an initial total temperature T_0 of 430 K. These conditions give a free-stream unit Reynolds number range of $0.4–18.3 \times 10^6$ m^{-1}, calculated using Keyes's law for viscosity (Keyes 1951). The maximum quiet stagnation pressure at the time of testing was approximately 1170 kPa which corresponds to a free-stream unit Re of 11.7×10^6 m^{-1}. The test-section diameter is 0.242 m at the nozzle exit, and the axisymmetric nozzle is 2.590 m long.

Obtaining quiet flow in a hypersonic tunnel is not a trivial task. The nozzle is polished to a mirror finish to avoid roughness-induced transition, and the contraction boundary layer is removed by bleed slots at the throat. A new laminar boundary layer then begins just upstream of the nozzle throat and is maintained through the test section. In addition, the air is filtered to remove dust or other particles above 0.01 μm that may damage the nozzle or trip the boundary layer. Under quiet-flow conditions, noise levels are 0.05 % or less (Steen 2010). The tunnel can also be run noisy if the bleed slots at the throat are kept closed. Noise levels vary from 2 % to 4.5 % under noisy-flow conditions. More details about the development of the BAM6QT can be found in Schneider (1998, 2000, 2008).

2.1.1. *Typical run conditions*

Typical run conditions are given in table 1. Many different runs were conducted for this work, but most were repeats of the nine listed conditions. These repeats had small variations in the initial total pressure of less than 1 % which contributed to run-to-run variation in Re of 1–2 %. Also, the driver tube of the tunnel was heated to 430 K, which was taken as the initial total temperature at the beginning of each run. Variations in the initial total temperature were less than 3 %. Isentropic relations were

https://doi.org/10.1017/jfm.2014.475 Published online by Cambridge University Press

Condition	$Re \times 10^6$ m^{-1}	M	P_0 (kPa)	T_0 (K)	p_∞ (kPa)
1	5.8	6.0	578	424	0.37
2	6.3	6.0	635	424	0.40
3	7.0	6.0	702	424	0.44
4	7.6	6.0	760	424	0.48
5	8.3	6.0	828	424	0.52
6	8.9	6.0	888	424	0.56
7	9.5	6.0	955	424	0.60
8	10.2	6.0	1021	424	0.65
9	10.8	6.0	1084	424	0.69

TABLE 1. Typical run conditions.

then used to compute the total temperature during the run by using the measured drop in total pressure. All nozzle-wall data were taken during the same time interval of a run ($t = 0.89$–1.39 s) to maintain a constant total temperature.

2.2. *Instrumentation*

Kulite XCQ-062-15A pressure transducers were used to measure surface pressure fluctuations on the BAM6QT nozzle wall. They have a resonant frequency of 225–300 kHz. The repeatability of the sensors is approximately 0.1 % of the full scale, or 0.1 kPa. The sensors have screens to protect the diaphragms from damage. For these tests, A-screen sensors were used, which simply have a large central hole. This screen offers only a small amount of diaphragm protection, but the sensor has a flat frequency response up to 30–40 % of the resonant frequency (Beresh *et al.* 2011). The sensitive area of the A-screen sensor is the hole size (0.81 mm^2).

The pressure transducers were only used to obtain the fluctuating signal. The nozzle-wall fluctuations were normalized by the free-stream pressure p_∞, computed using the total pressure and free-stream Mach number in the tunnel. Each sensor was statically calibrated using a Paroscientific Model 740 Standard quartz pressure transducer (reads 206 kPa full scale) as the pressure standard. The accuracy of the standard is better than 0.008 % of full scale. For diaphragm-type transducers, these static calibrations differ from dynamic calibrations by approximately 5 % (Raman 1974).

The signals from the pressure transducers were processed by custom-built electronics which supply a 10 V excitation using an integrated circuit (IC). The output signal was amplified by a gain of 100 with an INA103 instrumentation-amplifier IC. Tektronix TDS7104, DPO7104, two TDS5034B, and two DPO7054 digital phosphor oscilloscopes were used for data acquisition. The scopes have an 8-bit vertical resolution, but the resolution can be increased to over 12 bits in Hi-Res mode. Hi-Res mode is also used to provide digital filtering. The oscilloscopes average in real time at the maximum sampling rate of 1.25–5 GS s^{-1} (depending on the model) for four input channels and then save data at the specified sampling rate. This provides 3 dB of attenuation at 0.44 times the sampling frequency and more attenuation at higher frequencies. The data sampling rate for these measurements was typically 500 kHz. Pressure traces were post-processed by low-pass filtering the data at 175 kHz in MATLAB using an 8-pole digital Butterworth filter (48 dB of attenuation per octave). This filtering removes sensor diaphragm resonance from the pressure traces to show the underlying data more clearly.

https://doi.org/10.1017/jfm.2014.475 Published online by Cambridge University Press

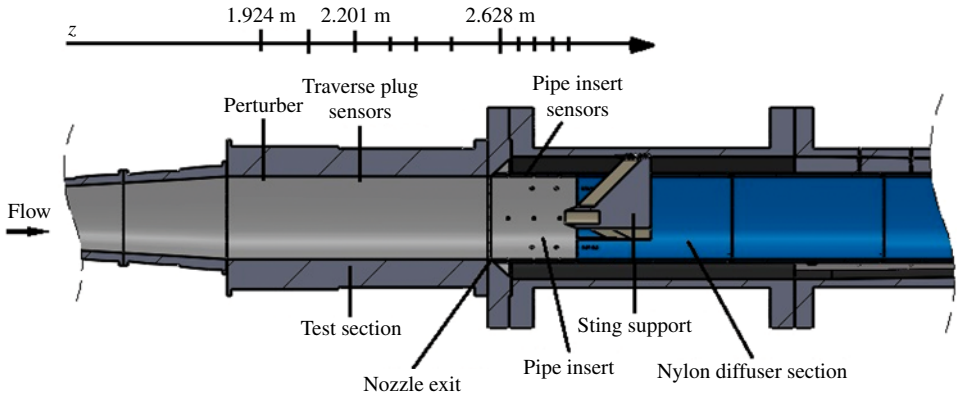


FIGURE 3. (Colour online) Schematic of experimental set-up in the BAM6QT for nozzle-wall measurements. Perturber and sensor locations are marked on the z axis.

2.3. *BAM6QT nozzle-wall set-up*

The axisymmetric Mach-6 quiet nozzle includes replaceable inserts in the nozzle wall. These inserts were used for perturber placement as well as for wall-mounted pressure transducers to study nozzle-wall disturbances. A schematic of the experimental set-up is shown in figure 3. The perturber was placed on the top wall of the tunnel in an upstream insert at $z = 1.924$ m, where z is the axial tunnel coordinate measured from the throat. There is also a small spanwise insert at $z = 2.055$ m, downstream of the perturber electrodes (figure 4*a*). Downstream, there is a slot in the top wall of the tunnel near the nozzle exit to allow traverse measurements with a Pitot probe or a hot wire. A traverse plug that has eight mounting holes for pressure sensors was fabricated to fill this slot (figure 4*a*). Pressure sensors were placed at four of these locations ($z = 2.201$, 2.302, 2.378, and 2.480 m).

Additional tunnel hardware was constructed to allow measurements downstream of the nozzle exit. Previous measurements showed that the nozzle-wall boundary layer appears laminar well downstream of the nozzle exit (Juliano *et al.* 2008; Steen 2010). To take advantage of this additional length of laminar flow, a cylindrical pipe insert was designed that fits between the nozzle exit and the diffuser sting support as shown in figures 3 and 4(*b*). This insert has the same diameter of 0.242 m as the nozzle exit. When the tunnel is closed, the pipe insert fits flush with the nozzle exit and extends 0.254 m downstream. This pipe insert is actually made of five rings with lap joints between them. The maximum step between the lap joints is approximately 20 μm and there is also a small streamwise gap between the edges for some ring configurations with a maximum width of 200 μm. These steps and gaps are small compared to the laminar boundary layer thickness (near 10 mm) and do not cause transition within the pipe insert.

Pressure sensors were typically located in each ring on the top wall of the pipe insert at $z = 2.628$, 2.679, 2.730, 2.781, and 2.831 m. These sensor locations are marked on the axis in figure 3 and are visible in figure 4(*b*). One of the rings has azimuthal sensor locations at $y = 0, \pm 11, \pm 21, \pm 32, \pm 42$, and ± 63 mm, where y is measured from the centreline of the perturber position clockwise along the circumference of the wall (looking upstream). The last four rings are interchangeable to allow azimuthal measurements at any of the four downstream locations.

https://doi.org/10.1017/jfm.2014.475 Published online by Cambridge University Press

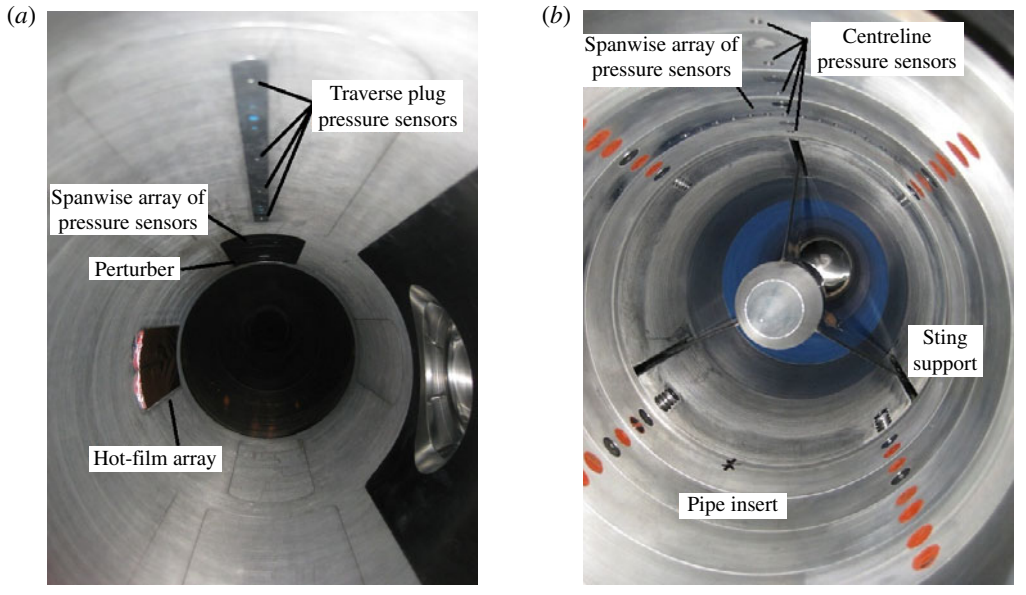


FIGURE 4. (Colour online) Nozzle-wall experimental set-up in the BAM6QT: (*a*) looking upstream from the nozzle exit; (*b*) looking downstream from the nozzle exit.

3. Flow perturbations using glow discharges

3.1. *Pulsed-glow perturber*

Controlled perturbations were introduced into the boundary layer of the BAM6QT to generate repeatable instability waves and turbulent spots farther downstream (Casper *et al.* 2011*a*,*b*, 2012; Casper 2012). A pulsed-glow perturber was developed using an automotive-type ignition coil and a timing circuit to create a perturbation across the electrodes. This perturber has an electrode design that isolates the ground from the tunnel to reduce electrical noise during perturbation generation (figure 5). This design has two 1.1 mm diameter stainless steel electrodes in a Macor mount. The axis of the two electrodes was placed perpendicular to the free-stream flow. The ignition coil remains energized until a perturbation is desired. Then, the coil is suddenly de-energized, and a perturbation is created. The perturber was typically pulsed at 200 Hz to allow measurements of the resulting disturbances in the intervals between the electromagnetic noise generated by the perturbation. The perturbation is turned off while the resulting disturbances convect downstream over the sensors. This pulsing creates a spacing of approximately 4 m between disturbances.

3.1.1. *Measurements of electrical perturbation*

To characterize the perturber behaviour, non-intrusive voltage and current measurements were made. The current across the electrodes was measured using a Bergoz CT-D1.0 current transformer as suggested by Bane (2010). The voltage between the electrode wires running from the perturber was measured using a Tektronix P6015 high-voltage probe. These measurements give the current and voltage of the perturbation as a function of time, allowing computation of the perturbation power. However, when making these measurements, there is the possibility of electro-magnetic interference which adds uncertainty to the results. The effect of this interference cannot be quantified with the present set-up.

https://doi.org/10.1017/jfm.2014.475 Published online by Cambridge University Press

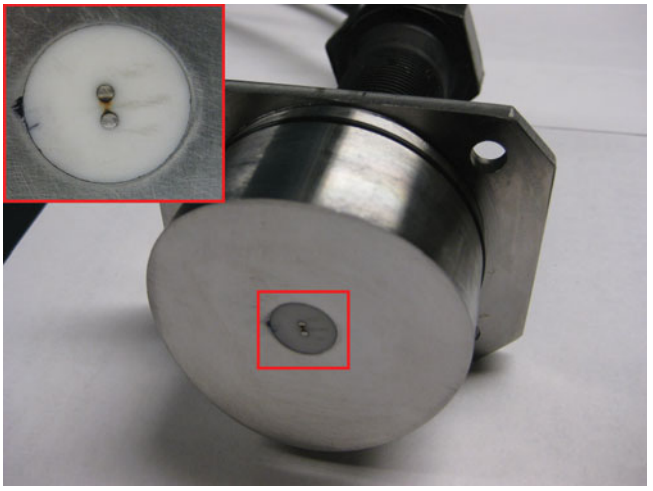


FIGURE 5. (Colour online) Perturber electrodes with isolated ground.

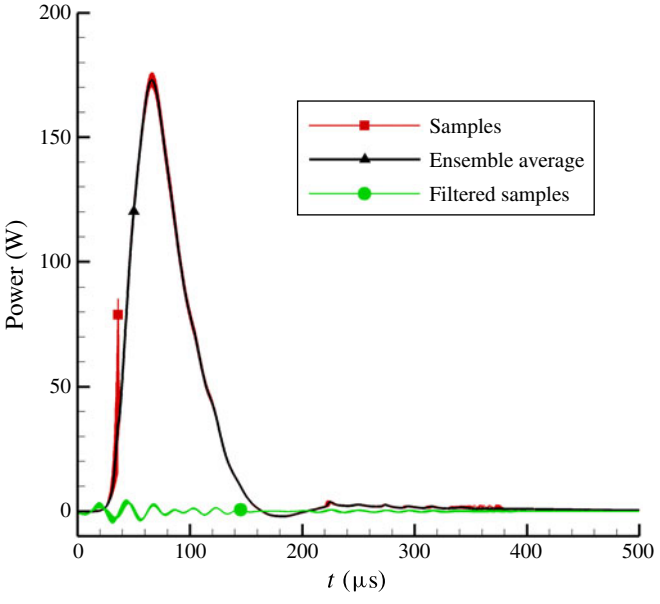


FIGURE 6. (Colour online) Power measurements of perturbation, individual samples, 30–60 kHz band-pass filtered samples and ensemble average, $Re = 10.8 \times 10^6$ m^{-1}.

Figure 6 shows typical power measurements. The ensemble average of 50 individual samples (trace with triangle symbol) shows a 200 μs pulse in power. The associated current and voltages lie in the expected range for a glow discharge (Ladoon 1998). The power spectral density (PSD) of the electrical perturbation was also computed to show its dominant frequency content (figure 7). Fast Fourier transforms (FFTs) of 50 perturbations were computed, and these were averaged and normalized to compute the PSD. The dominant frequencies in the spectra are below 30 kHz; however, there is frequency content that extends above 150 kHz. The amplitudes of these higher

https://doi.org/10.1017/jfm.2014.475 Published online by Cambridge University Press

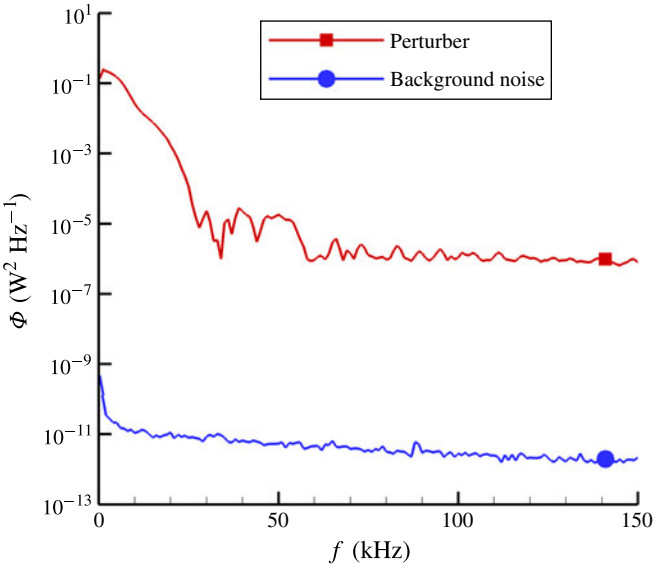


FIGURE 7. (Colour online) Power spectral density of power measurements at $Re = 6.40 \times 10^6$ m^{-1}.

frequencies are several orders of magnitude smaller than the low-frequency peak, but still much larger than the electronic noise in the system.

To investigate the component of the perturbation that would lead to boundary-layer instability growth, individual samples were band-pass filtered over the range of unstable second-mode wave frequencies on the nozzle wall (30–60 kHz). Fifty individual samples (traces with square symbol) and 50 band-pass filtered samples (traces with circle symbol) are shown along with the ensemble average in figure 6. As shown in the filtered traces, there is repeatable frequency content between 30 and 60 kHz during the glow pulse. The largest amplitude occurs during the initiation of the glow pulse when a rapid spike in the power is observed in the individual samples at around 30 μs. There is also some low-amplitude content between 250 and 400 μs. Boundary-layer disturbances are first measured downstream of the perturber at $z = 2.055$ m near $t = 200$ μs, so the source of the flow disturbances must occur before that time.

Although the perturber creates a pulsed glow, occasional superimposed sparks do occur as discussed in Casper (2012). These sparks initiate boundary-layer disturbances at a later stage of growth than that seen with an isolated glow pulse, but the subsequent evolution and structure of the disturbances appears the same in both cases. Moreover, a difficulty arises in that the number of sparks is not repeatable; a single trigger might result in as many as ten sparks combined with a single glow discharge. Also, the sparks generate large amounts of electrical noise that contaminates the measurements. Because of the non-repeatability of the sparks and the electrical noise generated by these perturbations, boundary-layer disturbances created by these sparks were not used. These large perturbations were identified using a threshold criterion and excluded from the data analysis. On the other hand, the glow perturbations that were used created controlled, repeatable perturbations on the nozzle wall without generating large amounts of electrical noise. The dominant frequency content of these glow pulses is below 30 kHz; however, there is also smaller broadband content at higher frequencies.

https://doi.org/10.1017/jfm.2014.475 Published online by Cambridge University Press

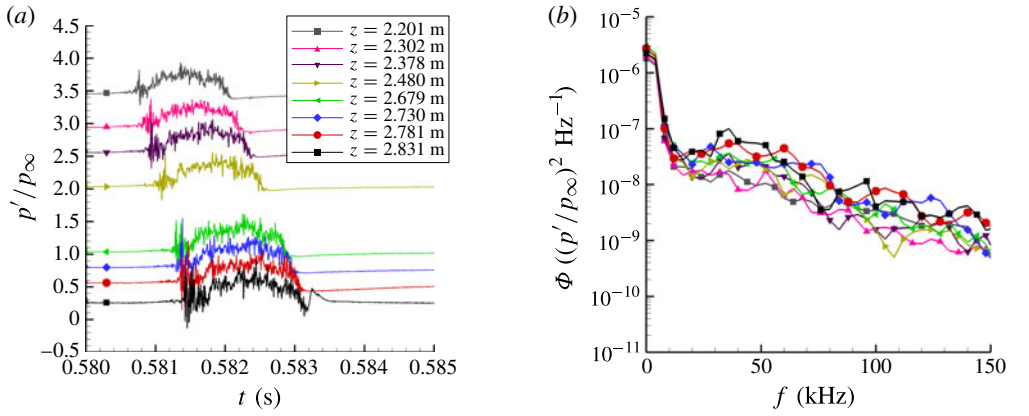


FIGURE 8. (Colour online) Large naturally developing turbulent region on the nozzle wall, $P_0 = 1142$ kPa, $T_0 = 428.3$ K, $Re = 11.2 \times 10^6$ m^{-1}. (*a*) Pressure traces, each trace is vertically offset proportional to z; (*b*) power spectral density.

4. Natural transition on the nozzle wall

4.1. *Streamwise measurements*

Under quiet-flow conditions, the nozzle boundary layer is predominantly laminar. This region of laminar flow extends at least 0.254 m past the nozzle exit, throughout the entire pipe insert. However, disturbances intermittently grow and break down in the laminar boundary layer. At an Re well below the maximum quiet Re, only a couple of disturbances might occur during a run. As the free-stream unit Reynolds number is increased, the disturbances occur more often (up to tens of disturbances per run). Above the maximum quiet free-stream unit Reynolds number, transition suddenly jumps toward the throat, and the boundary layer on the majority of the nozzle wall becomes turbulent. This sudden change probably occurs because roughness or some other disturbance near the throat becomes the dominant transition mechanism as the boundary layer thins with increasing unit Reynolds number.

Two types of disturbances are typically seen growing in the laminar boundary layer. The first are large turbulent regions that develop well upstream in the nozzle. By the time the disturbances pass over the sensors that are 2–3 m downstream, they are over 1 m long and cover most, if not all, of the nozzle circumference. These mature disturbances cannot be considered turbulent spots and do not display any of the structure associated with spots. Figure 8 shows typical pressure-fluctuation traces ($p' = p - p_\infty$) and the associated PSDs of one large turbulent region as it passes over the sensors on the top wall of the tunnel. These PSDs are created from one 0.05 s window segment containing the disturbances. Each trace is vertically offset from the upstream traces by an amount proportional to its axial tunnel location z to make the disturbance development clear. The sensor closest to the throat is offset the most, and the downstream sensors are offset to a lesser degree. Through the middle of the turbulent region, there is a higher average pressure as well as higher pressure fluctuations than in the undisturbed boundary layer. As the disturbance grows downstream, it elongates, but there is not a large change in the overall pressure fluctuations as indicated by the PSDs. Also, there is no evidence of instability waves within these disturbances. At the last sensor location ($z = 2.831$ m), a second pressure

https://doi.org/10.1017/jfm.2014.475 Published online by Cambridge University Press

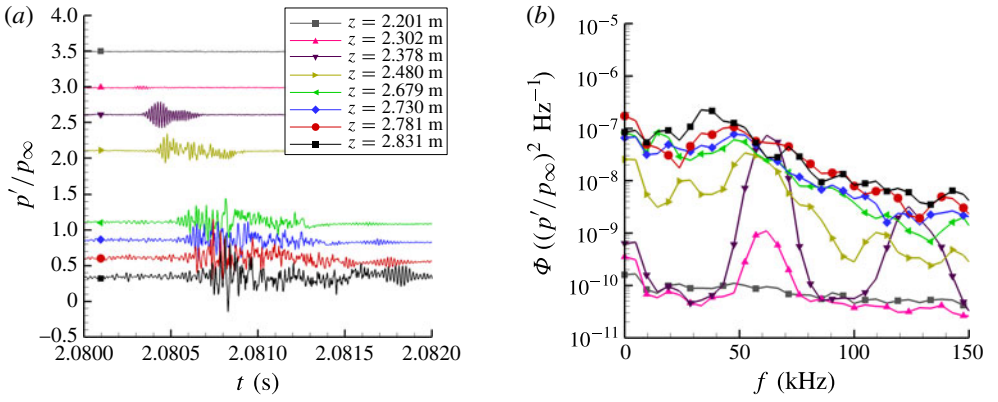


FIGURE 9. (Colour online) Growth of a small naturally developing turbulent spot on the nozzle wall, $P_0 = 1031$ kPa, $T_0 = 415.9$ K, $Re = 10.6 \times 10^6$ m^{-1}. (*a*) Pressure traces, each trace is vertically offset proportional to z; (*b*) power spectral density.

peak occurs just after the disturbance at $t = 0.5833$ s. This peak appears to be an upstream-travelling reflection of the disturbance from forward-facing steps (of the order of several mm) on either side of a sting-support slot that were located 0.0254 m downstream of the last sensor. This second pressure peak occurs only at the downstream end of the pipe insert and decays as it propagates upstream (Casper 2012). A new downstream diffuser section was later built to remove the forward-facing steps and move the sting-support slots farther downstream; it reduced the magnitude of this reflection in later tests.

The second type of natural disturbance typically measured is a wavepacket that breaks down into a turbulent spot along the nozzle wall. Figure 9(*a*) shows pressure traces of one such disturbance. Figure 9(*b*) shows the PSD of the pressure traces. In this case, a small wavepacket with a peak frequency near 62 kHz can be clearly seen at $z = 2.302$ m. The wavepacket is much larger and becomes nonlinear by $z = 2.378$ m, as indicated by the presence of a second harmonic. By the following sensor, the packet has begun to break down into a turbulent spot. This breakdown is seen in the PSD as a rise in broadband frequencies. As the spot propagates downstream, it continues to increase in size. Schneider (1998, 2000) performed instability computations at slightly lower *Re* during the design of the BAM6QT nozzle. Those computations indicated that the most amplified frequencies of second-mode waves in the nozzle boundary layer at the sensor locations are approximately 50–52 kHz (figure 33 in Schneider 1998). The present measurements are in good agreement with Schneider's computations, as they are taken at a slightly higher *Re* where the boundary layer would be thinner and lead to higher second-mode wave frequencies. These pressure traces also look qualitatively similar to DNS computations of wavepackets and turbulent spots in hypersonic flow (Sivasubramanian & Fasel 2010*a*). In this case, additional second-mode waves appear downstream of the spots by $z = 2.730$ m (figure 9*a*). However, the waves are not large enough to appear above the turbulent levels indicated in the PSD.

4.2. *Spanwise measurements*

The spanwise distributions of pressure fluctuations within these natural disturbances were also obtained at $z = 2.679$ m. These spanwise measurements were used to

https://doi.org/10.1017/jfm.2014.475 Published online by Cambridge University Press

create contour plots of the disturbances. Time traces of the pressure fluctuations were converted to an approximate streamwise coordinate $\tilde{z}$ using an average disturbance convection velocity ($\tilde{z} = -tU_c$). This convection velocity varied with Re between $0.79U_\infty$ and $0.84U_\infty$ (§ 5.4.2), where U_∞ is the free-stream velocity. On the nozzle wall, U_∞ is also the edge velocity U_e. The zero time origin for each case was picked to align the leading edges of the disturbances at $\tilde{z} = 0$ m. The leading edges were identified using the method of Hedley & Keffer (1974) described in § 5.4.2.

This conversion invokes Taylor's hypothesis which assumes the flow is 'frozen' as it convects over the sensor (Taylor 1938). This hypothesis is frequently used in the analysis of turbulent flow and has been shown to be a reasonable assumption for many cases, even for low-frequency fluctuations (Dennis & Nickels 2008). In the present case, the disturbances will grow in length as they convect over the sensors, but this conversion allows a reasonable approximation of the spatial footprint of the disturbances to be studied. When the time traces are converted to distance, a smaller time corresponds to a greater $\tilde{z}$ location. As a result, the front or leading edge of the disturbance corresponds to smaller t and larger $\tilde{z}$ while the rear or trailing edge corresponds to larger t and smaller $\tilde{z}$. References to 'upstream' and 'downstream' still correspond to the free-stream flow direction in the tunnel.

The zero-pressure contour lines were removed from the resulting contour plots and replaced by minimum contour lines at $\pm 0.05p'/p_\infty$ to compare the spanwise extent of the disturbances between varying Re. Other contour lines are displayed at intervals of $0.1p'/p_\infty$. The maximum and minimum pressure contour levels are changed for each case to better show the details of the disturbance structure.

Figure 10 shows examples of different nozzle wall disturbances at $z = 2.679$ m including a small wavepacket and developing turbulent spots. These disturbances appeared at different times during the same run. The small wavepacket is narrow in width and concentrated near its centre (figure 10*a*). Larger disturbances spread away from the centreline as the packets begin to develop into turbulent spots (figure 10*b–d*). These disturbances have the expected arrowhead shape of turbulent spots. Evidence of periodic second-mode waves is seen at the head and spanwise edges of the disturbances, but the remainder of the disturbances appears unorganized and turbulent. Behind each disturbance, a low-pressure region develops which corresponds to the typical 'calmed' region seen downstream of turbulent spots. This arrowhead shape and calmed region are consistent with low-speed studies (e.g. Schubauer & Klebanoff 1955). The characteristics of these natural wavepackets and spots will also later be shown to be similar to controlled disturbances created on the nozzle wall (§ 5).

5. Controlled perturbations on the nozzle wall

The origins of the naturally occurring disturbances on the nozzle wall and their spanwise locations relative to the line of sensors are unknown. It is difficult to study the growth and development of these disturbances because they are occurring in an uncontrolled fashion. To better study turbulent-spot pressure fluctuations, pulsed-glow perturbations were introduced in the boundary layer at a range of free-stream Re (§ 2.1.1).

Multiple disturbances were averaged to improve the signal-to-noise ratio. The averaging trigger was the 200 Hz square-wave input signal to the perturber. Ensemble-averaged pressure traces of a 3 ms time period after the glow were computed for 50 disturbances. These traces were chosen from a 0.5 s interval of a run, after the perturber had been running for a few tenths of a second. More

https://doi.org/10.1017/jfm.2014.475 Published online by Cambridge University Press

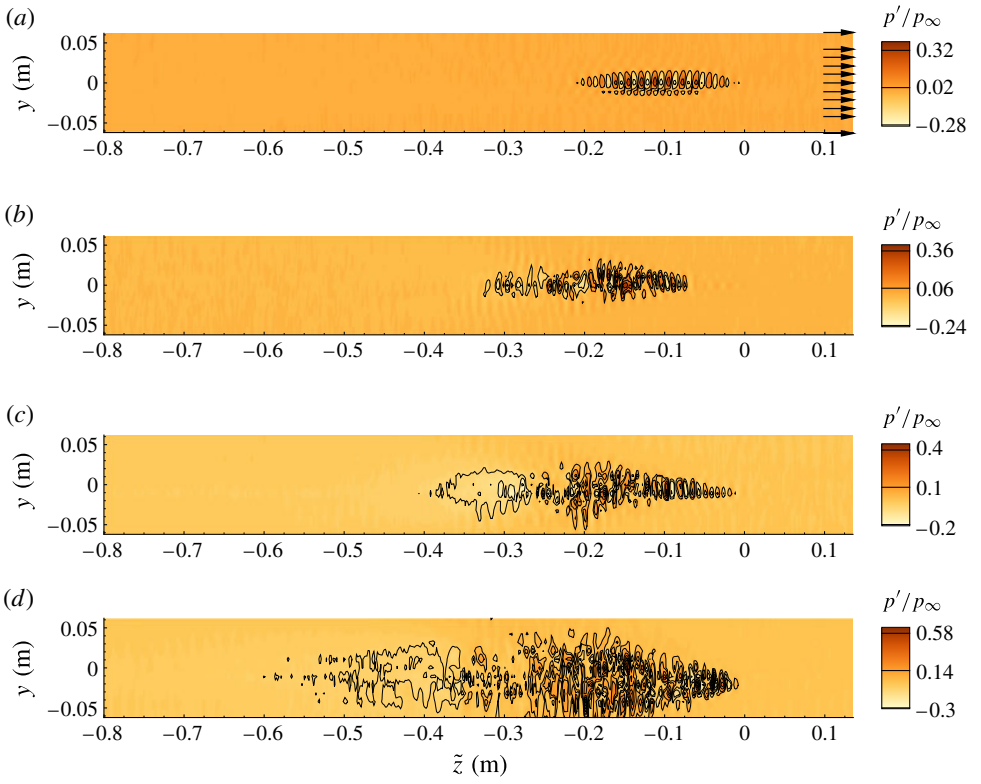


FIGURE 10. (Colour online) Contour plots of the pressure distribution within different natural disturbances on the nozzle wall, $Re = 10.8 \times 10^6$ m^{-1}, $z = 2.679$ m. (*a*) Small wavepacket, arrows on the right-hand axis mark the location of the spanwise sensors; (*b–d*) developing turbulent spots.

repeatable results were obtained after the perturber had warmed up. Also, even though Re drops within this 0.5 s interval, the change was smaller than 4 % and no noticeable effects were seen in the results.

Any disturbances that were contaminated by naturally occurring turbulent spots or electrical noise from occasional spark discharges were not used in the averages. These cases occurred infrequently and were identified using a root-mean-square (RMS) threshold criterion on the laminar-boundary-layer data measured by a single sensor between glow-induced disturbances. A nozzle-wall sensor at $z = 2.055$ or 2.201 m was typically used for this check since glow-induced disturbances were still small, and the majority of the measured pressure traces contained undisturbed laminar-boundary-layer data.

An ensemble-averaged PSD was also computed by averaging together the FFT of each of the 3 ms pressure traces and normalizing to obtain the PSD. This ensemble-averaged PSD is not the same as taking a PSD of the ensemble-averaged pressure traces. This difference is most apparent when wavepackets begin to break down to turbulence. Even though the packets show good repeatability while growing, their breakdown varies from packet to packet, and the pressure fluctuations are no longer in phase. As a result, the ensemble-averaged pressure traces smooth out the turbulent fluctuations seen during breakdown. Since phase information is not contained

https://doi.org/10.1017/jfm.2014.475 Published online by Cambridge University Press

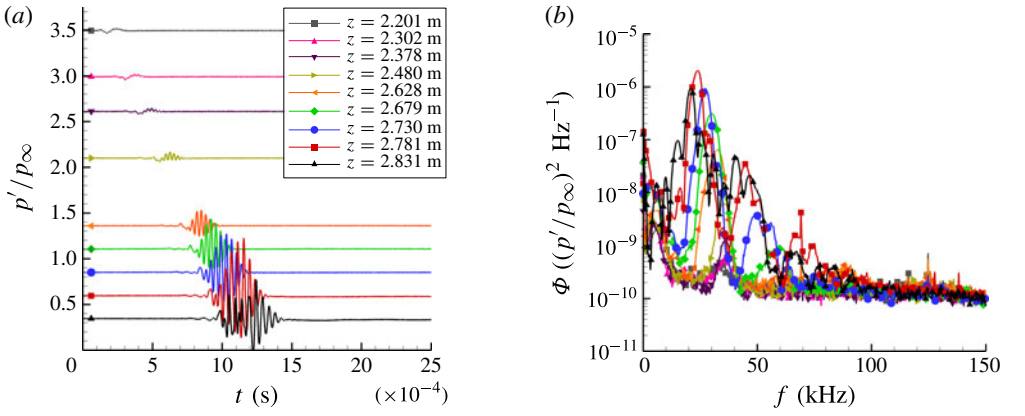


FIGURE 11. (Colour online) Centreline measurements of ensemble-averaged disturbances from pulsed-glow perturbations, $Re = 6.33 \times 10^6$ m^{-1}. (*a*) Pressure traces, each trace is vertically offset proportional to z; (*b*) power spectral density.

in the FFT, ensemble averaging FFTs does not remove the large fluctuations during breakdown but instead creates an average representation of the frequency content of the individual samples.

5.1. *Streamwise centreline measurements*

Figures 11–13 show ensemble-averaged pressure-fluctuation traces and PSDs of the controlled disturbances over a range of free-stream conditions. At the lowest free-stream Reynolds number of 6.33×10^6 m^{-1} (figure 11), a small wavepacket develops and grows over the measurement region. The peak frequency decreases from 36 to 21 kHz as the boundary layer thickens downstream. This wavepacket is the second-mode instability which acts like a trapped acoustic wave in the boundary layer. As a result, the frequency of the second-mode waves is inversely proportional to the boundary-layer thickness. Up to $z = 2.628$ m, the wavepacket is small and appears linear, as evidenced by the lack of any harmonics in the PSD. Farther downstream, the wavepacket becomes nonlinear as indicated by the presence of harmonics in the PSD. For example, at $z = 2.679$ m, there is a single harmonic in the spectra at 60 kHz. At $z = 2.781$ m, harmonics are visible at 44 and 66 kHz, respectively. Once the nonlinear waves become large enough, other peaks appear in the spectra above and below the fundamental frequency and its harmonics. For example, additional peaks at $z = 2.781$ m are visible at 7, 16, 29, 34, and 51 kHz, among others. These additional peaks appear to be generated by nonlinear wave interactions (Kimmel & Kendall 1991).

As *Re* is increased, the amplitude of the initial disturbance also increases and the waves become nonlinear farther upstream (figure 12). Large nonlinear harmonics are seen in the PSD, in addition to the fundamental second-mode peak. These harmonics can be very large and in some cases are higher than the broadband frequencies seen after breakdown. This is particularly evident at $z = 2.730$ m. Near $z = 2.781$ m, the wavepackets break down to turbulence. This breakdown is clearly seen in the PSDs. The amplitude of the primary second-mode frequency decreases, and the broadband amplitude rises. Also, as turbulence is approached, positive pressure excursions are greater in magnitude than the negative ones.

https://doi.org/10.1017/jfm.2014.475 Published online by Cambridge University Press

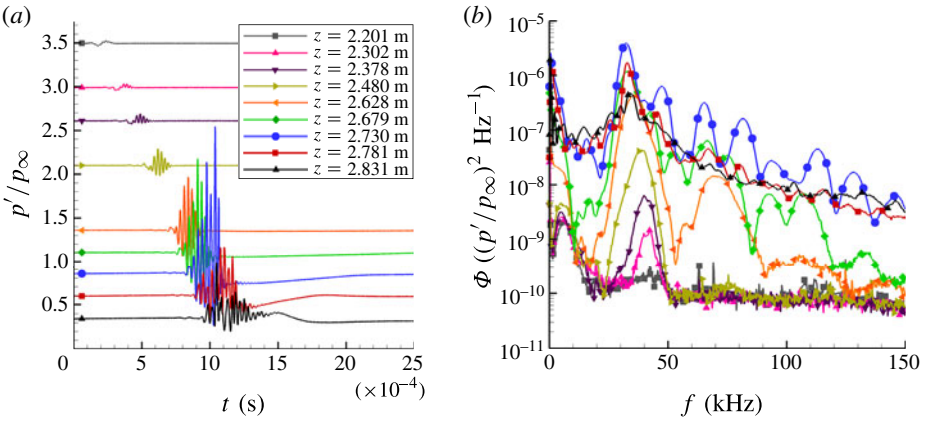


FIGURE 12. (Colour online) As figure 11, but for $Re = 8.25 \times 10^6$ m^{-1}.

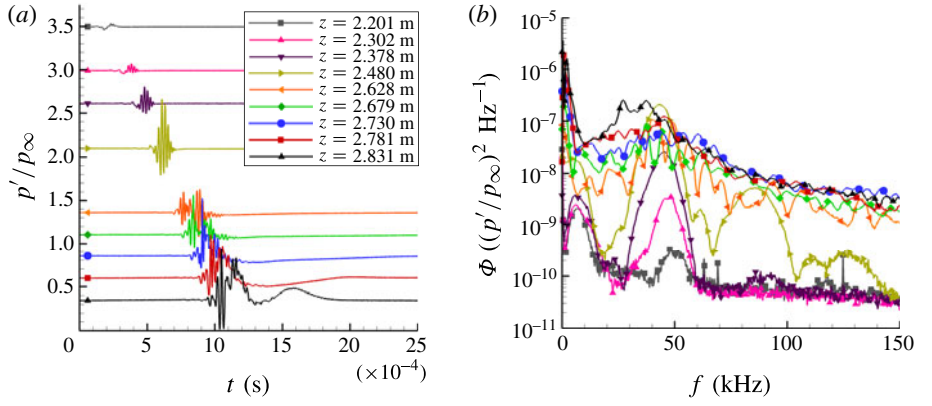


FIGURE 13. (Colour online) As figure 11, but for $Re = 10.8 \times 10^6$ m^{-1}.

At the highest Re of 10.8×10^6 m^{-1} (figure 13), the free-stream conditions are similar to the naturally occurring disturbances discussed in § 4. A wavepacket is initially generated by the pulsed-glow perturbation. The wavepacket grows downstream, and its peak frequency decreases from 50 to 43 kHz. These frequencies are lower than the peak frequency seen in natural disturbance growth at similar conditions and are likely to be due to the reduced distance, or fetch, for wave growth. The disturbance is introduced well downstream in the nozzle at $z = 1.924$ m, where the boundary layer is much thicker than near the throat. Farther downstream, the wavepacket becomes nonlinear and breaks down into a turbulent spot by $z = 2.679$ m. At $z = 2.730$ and 2.831 m, a second pressure rise behind the turbulent spot is seen at $t = 0.002$ and 0.001 55 s, respectively. As mentioned earlier, this second pressure rise seems to be generated when the turbulent spot passes two forward-facing steps on the nozzle wall. The reflection propagates upstream at subsonic speed and rapidly decays.

In these disturbances, breakdown occurs first in the middle of the packet. Second-mode waves are still visible in front of and behind the breakdown region. As the spot grows, the turbulent region lengthens. However, there is still evidence of the

https://doi.org/10.1017/jfm.2014.475 Published online by Cambridge University Press

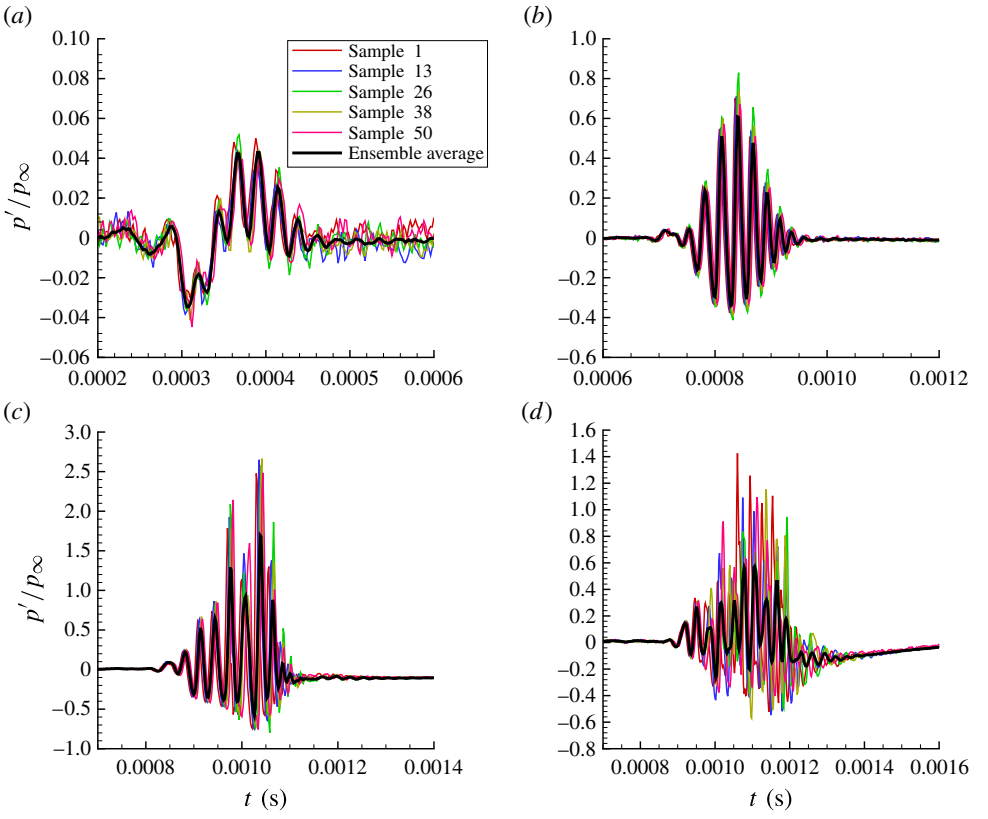


FIGURE 14. (Colour online) Comparison of individual pulsed-glow samples to the ensemble average, $Re = 8.25 \times 10^6$ m^{-1}: (*a*) $z = 2.302$ m; (*b*) $z = 2.628$ m; (*c*) $z = 2.730$ m; (*d*) $z = 2.831$ m.

second-mode waves in the front and rear of the spot. There is no sudden transition from instability waves to turbulent fluctuations. Instead there is a gradual growth and breakdown of the second-mode waves into turbulent spots. As a result, there is a long region where instability waves are seen while turbulent fluctuations are observed growing within the spot.

5.2. *Repeatability of controlled disturbances*

The deviation of the individual samples from the ensemble average is important when studying the averaged results. As the wavepackets grow, become nonlinear, and break down to turbulence, the individual samples will no longer repeat, and the ensemble average will not be a good representation of the individual samples. Figure 14 shows five individual samples as well as the ensemble average acquired from all fifty samples generated by a pulsed-glow perturbation. At $z = 2.302$ m, the disturbance is still small and shows good repeatability. As the disturbance grows, the variation from sample to sample increases, but there is still good repeatability. By $z = 2.730$ m, the packets have begun to break down. The ensemble average still represents the individual samples well, but the variation between individual samples and the ensemble average is much greater. By $z = 2.831$ m, the ensemble average no longer represents the individual time

https://doi.org/10.1017/jfm.2014.475 Published online by Cambridge University Press

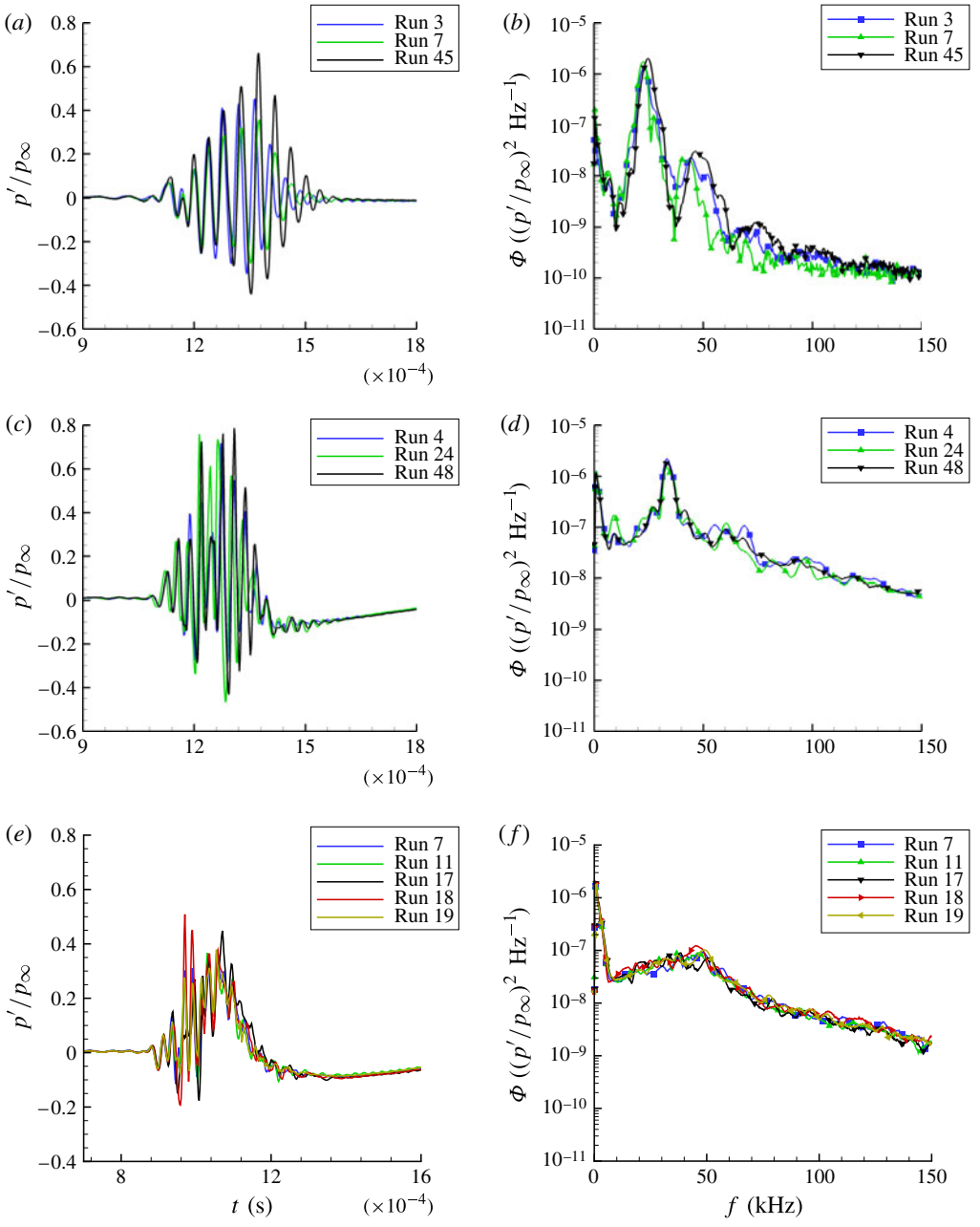


FIGURE 15. (Colour online) Repeatability of pulsed-glow ensemble averages, $z = 2.781$ m: (*a*,*c*,*e*) pressure traces at $Re = 6.40$, 8.40 and 10.8×10^6 m^{-1}, respectively; (*b*,*d*,*f*) power spectral density at $Re = 6.40$, 8.40 and 10.8×10^6 m^{-1}, respectively.

traces. Each sample has broken down to turbulence in a different manner. As a result, the ensemble average hides the true turbulent fluctuations present within the spot.

The repeatability of the boundary-layer disturbances is important for interpreting the results and comparing to DNS computations. Repeat runs were conducted to account for sensor precision uncertainties as well as the repeatability of the flow in the tunnel.

https://doi.org/10.1017/jfm.2014.475 Published online by Cambridge University Press

$Re \times 10^6$ m^{-1}	Coefficient of variation (%)
6.4	8.4
8.4	4.1
10.8	2.0

TABLE 2. Coefficient of variation (standard deviation/mean $\times$ 100) for repeat runs at varying Re, $z = 2.781$ m.

Figure 15 shows ensemble-averaged pressure traces as well as the PSDs for repeat runs at $z = 2.781$ m, for varying Re. The ensemble-averaged pressure traces have similar average pressure variations from run to run, and the PSDs also show similar frequency content.

To quantify the repeatability of these results, the variability between runs was computed (table 2). First, the average RMS of the fifty samples used in the ensemble averages was computed for each repeat run. Then, the mean and standard deviation of these values was calculated. Finally, the coefficient of variation was found (standard deviation/mean $\times$ 100). The highest variability of 8.4 % was found for the results at a low Re of 6.40×10^6 m^{-1}. The waves are large and nonlinear at this condition, so there is more variability in the average RMS level between runs. At higher Re, the waves have broken down to turbulence. Although the sample-to-sample variability has increased, the average RMS levels of the samples show less variability. This is because the samples are statistically similar.

5.3. *Spanwise measurements*

Spanwise measurements of the pulsed-glow disturbances were also made between $z = 2.679$ and 2.831 m. Figure 16 shows contour plots of the ensemble-averaged spanwise pressure fluctuation at a lower free-stream Re of 6.40×10^6 m^{-1}. Detailed pressure traces and PSDs may be found in Casper *et al.* (2011*b*) and Casper (2012). As in § 4.2, time traces were converted to a spatial coordinate using Taylor's hypothesis. At $z = 2.679$ m, the wavepacket is clearly seen as alternating lines of positive and negative pressure fluctuations. However, the fluctuations tend to have a greater positive magnitude than negative, especially as they grow larger, which was seen in the streamwise measurements. These fluctuations are concentrated near the centre of the disturbance and occur in a periodic and organized fashion. There are also weak disturbances spreading obliquely in the spanwise direction. At this point, the wavepacket already shows nonlinearity along the centreline as indicated by the presence of a second harmonic in the spectra (figure 11*b*). Farther downstream, the large fluctuations of the wavepacket are still concentrated near the centreline; however, the packet is becoming distorted. The wavefronts have started to propagate along spanwise lines, and weaker disturbances are seen spreading farther afield along the same angle. It appears that the wavepacket is beginning to show evidence of breakdown and is developing some characteristics of a turbulent spot.

At a higher Re near 8.30×10^6 m^{-1}, a similar development of a second-mode wavepacket is seen. However, growth and breakdown of the waves happens farther upstream, allowing the continued breakdown of the waves and development of turbulent spots near the end of the measurement region where the spanwise sensors are located. Contour plots at the four downstream measurement locations show the pressure-fluctuation field within a typical disturbance as it breaks down into a turbulent

https://doi.org/10.1017/jfm.2014.475 Published online by Cambridge University Press

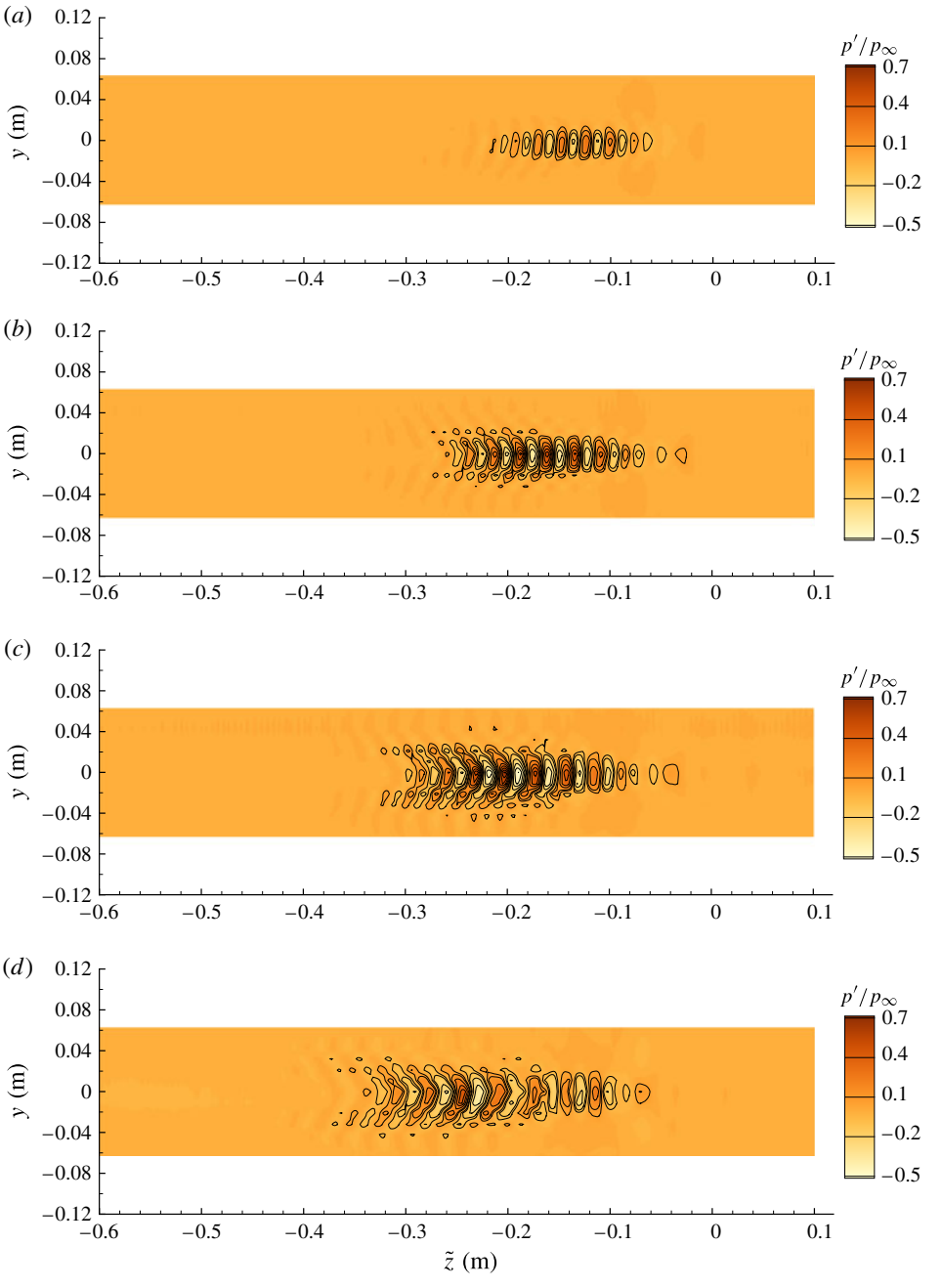


FIGURE 16. (Colour online) Contour plots of ensemble-averaged disturbances, $Re = 6.35$–6.38×10^6 m^{-1}: (*a*) $z = 2.679$ m; (*b*) $z = 2.730$ m; (*c*) $z = 2.781$ m; (*d*) $z = 2.831$ m.

spot (figure 17). For the measurements at $z = 2.679$ m, the second-mode wavepacket is still contained near the centreline. Farther downstream, the disturbance footprint still clearly shows the second-mode waves, but they have spread in the spanwise direction and become distorted. The spanwise edges of the wavepacket are also jagged. By

https://doi.org/10.1017/jfm.2014.475 Published online by Cambridge University Press

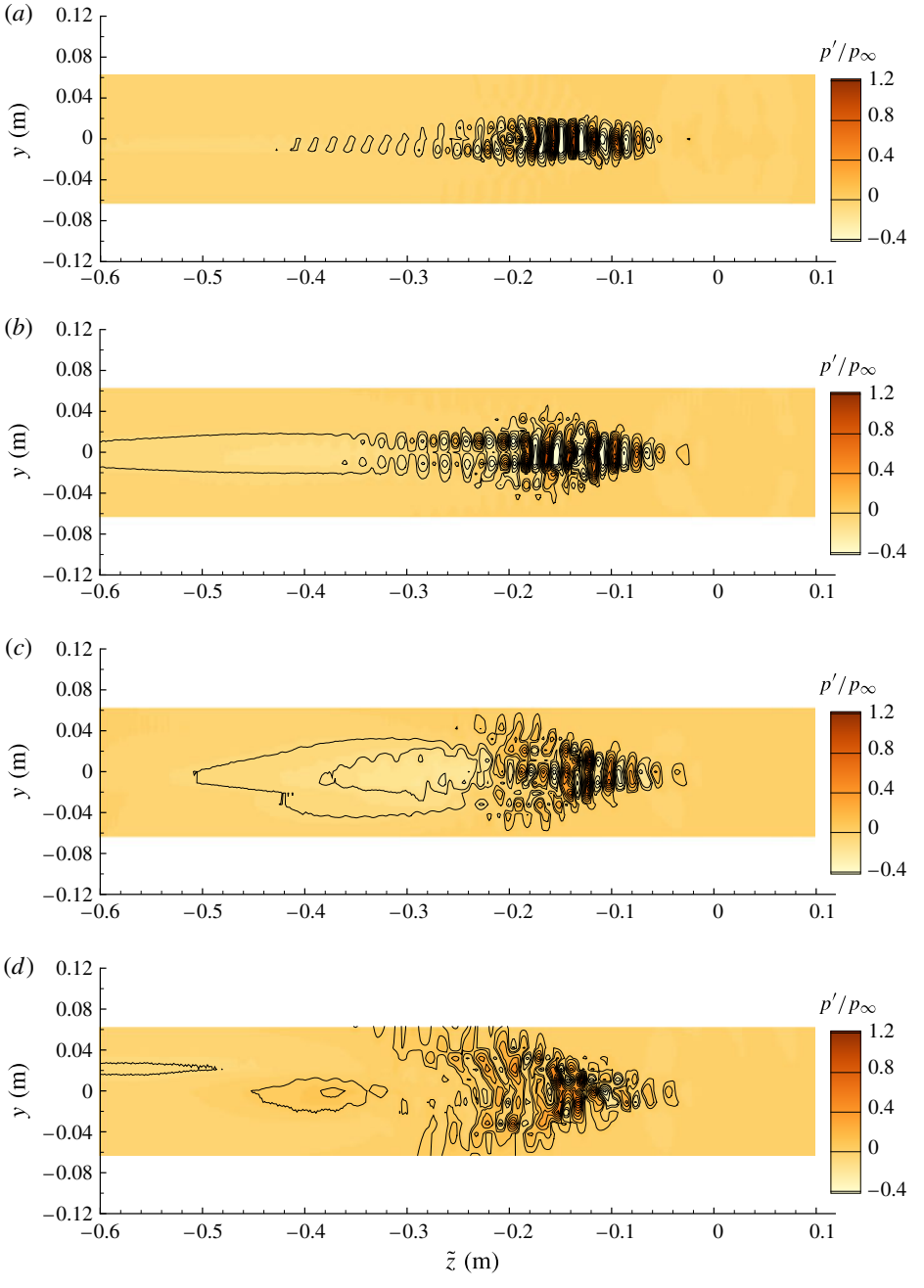


FIGURE 17. (Colour online) Contour plots of ensemble-averaged disturbances, $Re = 8.32\text{–}8.34 \times 10^6$ m^{-1}: (*a*) $z = 2.679$ m; (*b*) $z = 2.730$ m; (*c*) $z = 2.781$ m; (*d*) $z = 2.831$ m.

$z = 2.831$ m, the spanwise spread of larger disturbances is evident and the characteristic arrowhead shape of the turbulent spots can be seen; however, it is unclear at which point the wavepacket becomes a turbulent spot. There is a gradual change between the two cases. Breakdown of the waves occurs first on the centreline where the wave

https://doi.org/10.1017/jfm.2014.475 Published online by Cambridge University Press

amplitudes are largest. However, traces of the second-mode waves can still be seen, especially at the front and rear of the disturbances as well as in the spanwise edges.

Another feature at this *Re* is a lower-pressure region downstream of the disturbances. This low-pressure calmed region is a feature of typical turbulent spots (§ 1). In this case, the large wavepackets also begin to show a calmed low-pressure region. However at $z = 2.831$ m (figure 17*d*), the low-pressure region can barely be seen and there is a second positive pressure peak. As discussed in § 4, this second pressure peak is a reflection of the disturbance from a step downstream of this sensor and is not a physical part of the turbulent spot. This reflection masks the presence of the calmed region downstream of the disturbances at this sensor location only.

The spanwise width of the waves can be compared to the coherence measurements by Kimmel, Demetriades & Donaldson (1995) under conventional noise levels. They found that the spanwise coherence of second-mode waves was approximately four times the boundary-layer thickness δ. In the present quiet-flow case, the boundary layer was computed to be 9 mm thick at the nozzle exit. This computation was done using a finite-difference boundary-layer analysis (Harris & Blanchard 1982) which has been shown to work well for computing the boundary layer in the BAM6QT under quiet-flow conditions (Wheaton 2009). The width of the packets remains approximately within 4δ until $z = 2.781$ m when the waves begin to break down and stronger disturbances spread in the spanwise direction.

Figure 18 shows contour plots of the pressure fluctuations at the highest *Re* of 10.8×10^6 m^{-1}. A turbulent spot has developed by $z = 2.679$ m. Farther downstream, the spot grows larger and spreads in the spanwise direction. Behind the spot, a negative pressure-fluctuation region is seen which corresponds to a typical 'calmed' region. Some evidence of second-mode waves appears in this calmed region and is most clear in figure 18(*b*). Second-mode waves also persist at the front and at the spanwise edges of the spot.

The measurements do not vary significantly with downstream distance, consistent with the turbulent regime being reached. The turbulent core does increase in size in the streamwise and spanwise directions, as indicated by the lack of periodicity and distortion of the pressure-fluctuation field and broadband frequency components in the PSDs. However, second-mode waves are still observed at the spanwise edges of the spot.

These measurements show the gradual evolution of a second-mode instability wavepacket into a young turbulent spot in a hypersonic boundary layer. At hypersonic speeds, the instability waves and turbulent spots coexist during the transition process. Turbulent spots still show evidence of the second-mode instability in the front and spanwise edges of the spots, as well as in the calmed region downstream of the spots. This intermixing of waves with turbulence appears different to what is seen for low-speed and supersonic results, which show a turbulent core without evidence of instability waves (James 1958; Riley & Gad-el Hak 1984; Fiala *et al.* 2006), though some rare exceptions in an adverse pressure gradient have been found (Seifert & Wygnanski 1995). This difference in the structure of the spots is consistent with DNS results that show a change in the character of the spots from supersonic results up to about Mach 4 to hypersonic results at Mach 5–6 (Krishnan & Sandham 2006*b*; Joksch & Kleiser 2008; Redford *et al.* 2012). Recent DNS results also show a similar character for turbulent spots on a cone at Mach 6 (Sivasubramanian & Fasel 2010*a*).

5.4. *Turbulent spot model development and experimental inputs*

As discussed in § 1, a turbulent spot model of the transition process relies on several experimental parameters. Some of these parameters may be estimated based on the

https://doi.org/10.1017/jfm.2014.475 Published online by Cambridge University Press

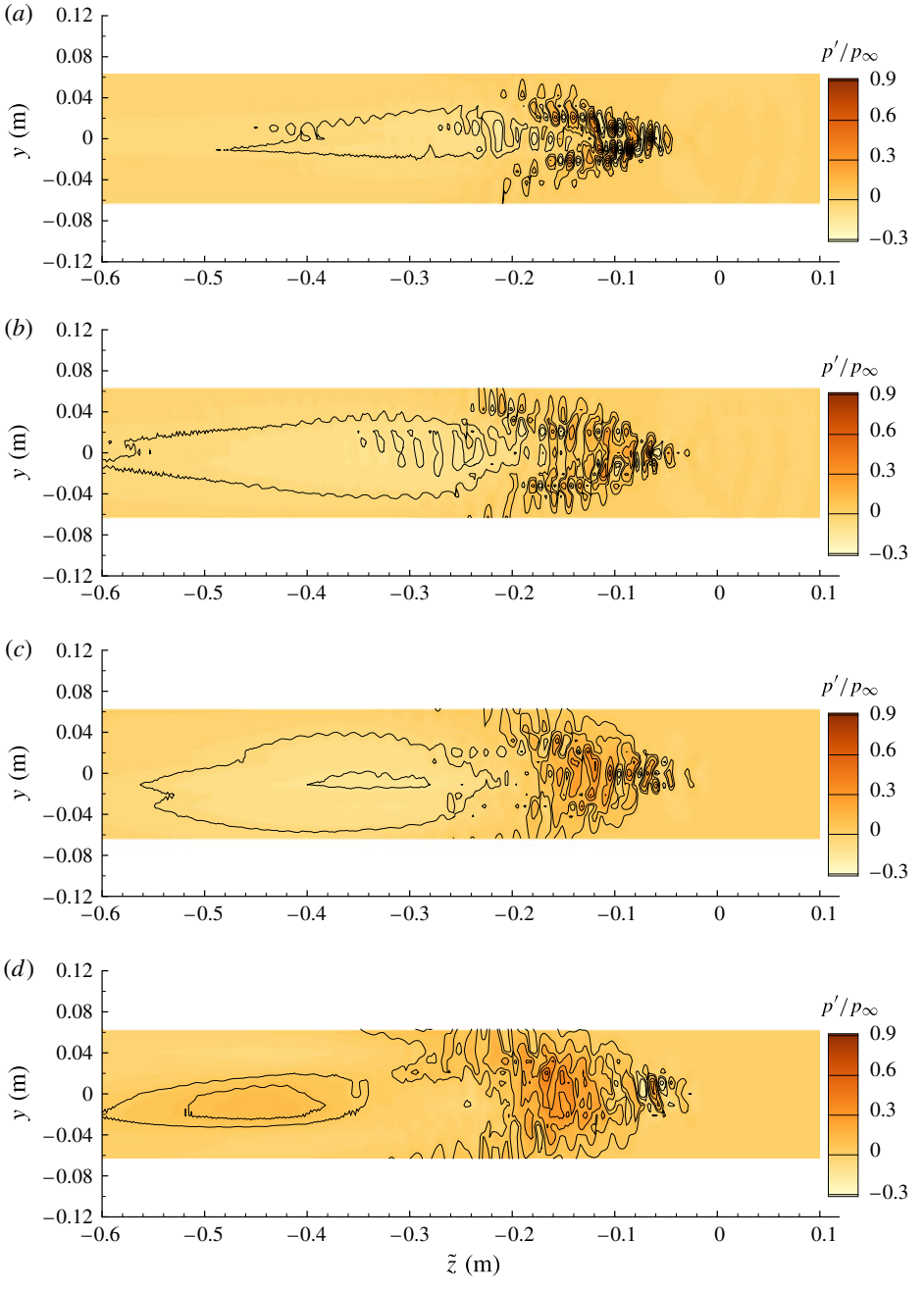


FIGURE 18. (Colour online) Contour plots of ensemble-averaged disturbances, $Re = 10.7\text{–}10.9 \times 10^6$ m^{-1}: (*a*) $z = 2.679$ m; (*b*) $z = 2.730$ m; (*c*) $z = 2.781$ m; (*d*) $z = 2.831$ m.

present experimental results, including the internal pressure field of the disturbances as well as the spot growth parameters. The internal pressure of spots consists of two parts. There is an elevated pressure within the disturbances superposed on which are higher-frequency fluctuating components. The low-frequency component may be examined by low-pass filtering the present data. These lower frequencies are nearer

https://doi.org/10.1017/jfm.2014.475 Published online by Cambridge University Press

the typical frequencies of structural vibration. The higher-frequency component of the pressure was addressed previously with PSDs of the disturbances. In addition, spot growth parameters including the convection velocity and the lateral spreading half-angle of the spot must be incorporated into a turbulent spot model. These values may be derived from the present data.

The way that spots merge and interact must also be known. Classic intermittency models assume that the merging of two spots creates a larger turbulent region described by the superposition of the individual areas covered by the spots, assuming no interaction. However, low-speed experiments and recent DNS have shown that there may actually be an interaction (Zilberman, Wygnanski & Kaplan 1977; Savas 1979; Gutmark & Blackwelder 1987; Makita & Nishizawa 2001; Krishnan & Sandham 2006*b*). In the longitudinal merging case, the downstream spot may be suppressed (Gutmark & Blackwelder 1987; Krishnan & Sandham 2006*b*). In the lateral merging cases, fluctuations may be enhanced at the interacting wing tips (Makita & Nishizawa 2001; Krishnan & Sandham 2006*b*). The present work does not address this disturbance merging, but some preliminary results are discussed in Casper (2012) and Casper *et al.* (2012).

5.4.1. *Low-frequency disturbance field*

The low-frequency content of the disturbances was found by low-pass filtering the traces at 15 kHz using an eighth-order Butterworth filter. This frequency cutoff was chosen to be below the lowest second-mode wave frequency observed at $Re = 6.40 \times 10^6$ m^{-1}. At this low Re, there was not any significant low-frequency content in the wavepackets. However, at higher Re, an elevated pressure is seen in the middle of the disturbances. Figure 19 shows contour plots of the filtered disturbances at an intermediate Re of 8.40×10^6 m^{-1}. At $z = 2.679$ m, there is only a small region of higher pressure concentrated near the centreline. This higher pressure region corresponds to a part of the second-mode wavepacket that has begun to distort. Downstream there is a long region of low pressure which is probably the beginning of the development of a calmed region behind the disturbances.

These high- and low-pressure regions grow in area farther downstream. By $z = 2.781$ m, the high-pressure region has begun to form an arrowhead shape with a peak pressure approximately 40 % above the free-stream pressure. However, in this case, the front of the arrowhead is missing. This front region is dominated by second-mode waves as shown in figure 17. Behind these ordered waves, there is a distorted region that appears turbulent and corresponds well with the higher pressure region in these low-frequency plots. Downstream of this high pressure, the calmed low-pressure region has also spread from the centre and has a peak amplitude approximately 20 % below p_∞.

Similar results are obtained at the highest Re of 10.8×10^6 m^{-1} (figure 20). The disturbances all appear as turbulent spots, especially downstream of $z = 2.679$ m (figure 18). The elevated pressure within the disturbances can be seen and has a roughly triangular arrowhead shape. This elevated pressure is about a third above the free-stream pressure. The calmed region behind the spot is much longer and has an average pressure approximately 10 % below p_∞.

These plots show that the low frequencies can help indicate distortion of ordered second-mode structure and the beginning of turbulence development within the disturbances. At low Re, when only wavepackets are present, the low frequencies are small. As the waves grow larger and begin to distort, elevated pressures begin to appear in the disturbances and a low-pressure calmed region begins to form

https://doi.org/10.1017/jfm.2014.475 Published online by Cambridge University Press

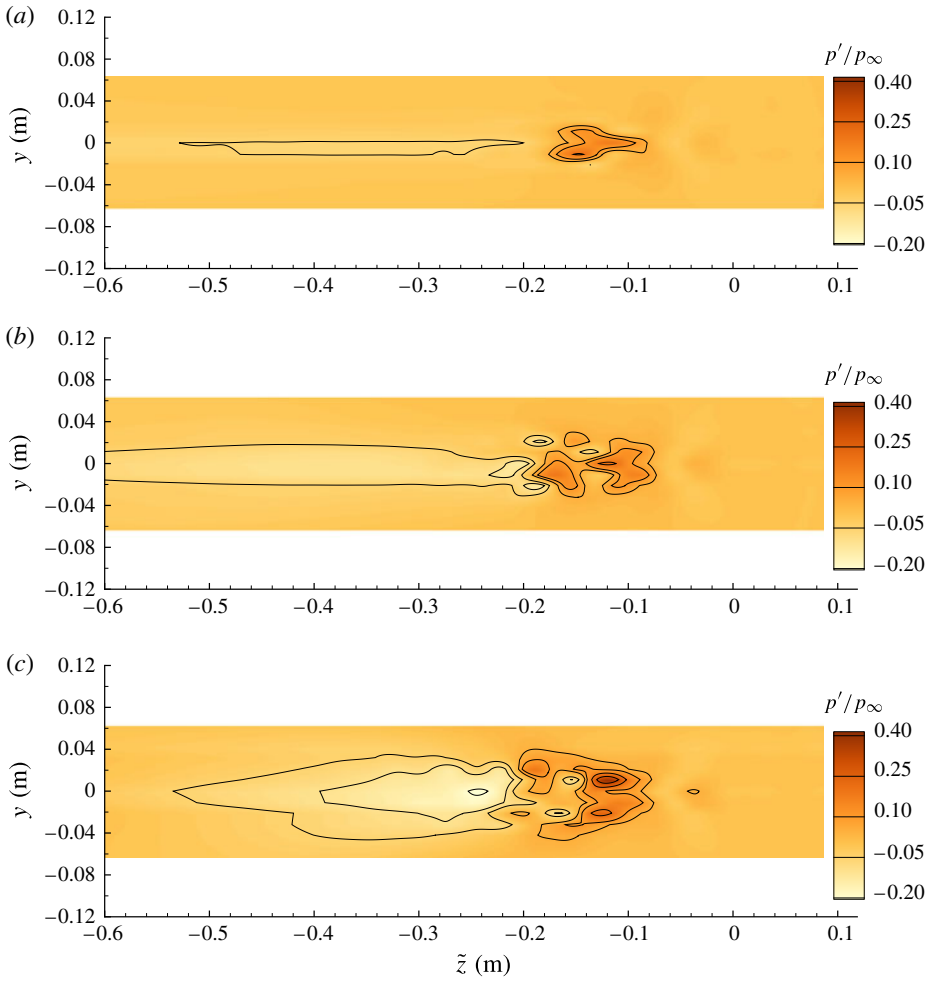


FIGURE 19. (Colour online) Contour plots of spanwise measurements, low-pass filtered traces, $Re = 8.32\text{–}8.34 \times 10^6$ m^{-1}: (*a*) $z = 2.679$ m; (*b*) $z = 2.730$ m; (*c*) $z = 2.781$ m.

downstream. As turbulent spots develop, this region of elevated pressure grows larger and forms a typical arrowhead shape. Downstream, the low-pressure calmed region also grows larger as the turbulent spots form. It may be that this calmed region plays an important role for modelling transitional fluctuations. Even though the low-pressure region has a lower amplitude, it has a much larger extent than the elevated pressure in the spots. Therefore, this calmed region increases the overall change in pressure when spots pass by.

5.4.2. *Convection velocity of wavepackets and turbulent spots*

A direct determination of the convection velocity for the wavepackets and turbulent spots can be made by analysing the pressure traces. Hedley & Keffer (1974) generalized a procedure to differentiate turbulent and non-turbulent flow. The procedure takes an intermittent signal and first sensitizes it by using a detector function. This function differentiates and squares the signal to emphasize the

https://doi.org/10.1017/jfm.2014.475 Published online by Cambridge University Press

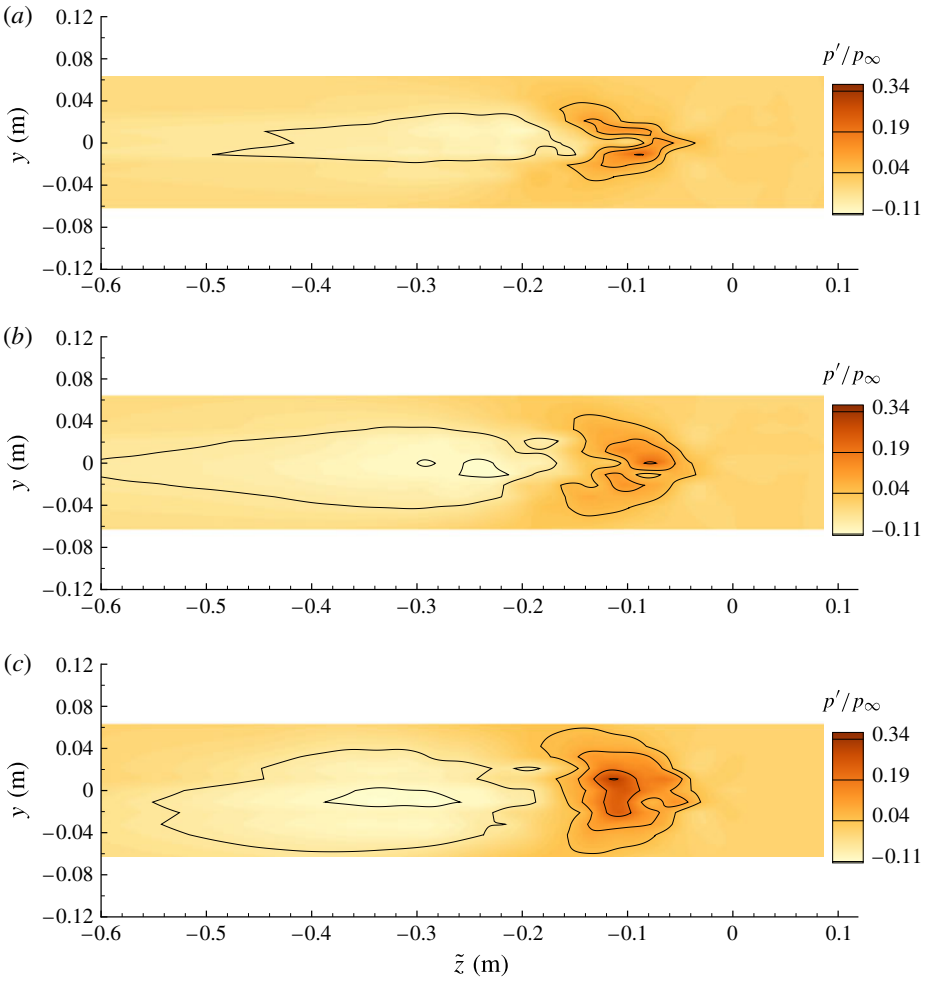


FIGURE 20. (Colour online) As figure 19, but for $Re = 10.7\text{–}10.9 \times 10^6$ m^{-1}.

high-frequency components. This function is then smoothed by averaging over a short time interval to create a criterion function. This removes any zeros that are part of the turbulence and would otherwise signal the end of a turbulent region. The final step is to set a threshold level. Above the threshold, the flow is considered turbulent and below it, the flow is considered laminar. By applying this threshold, an indicator function consisting of ones (for turbulent flow) and zeros (for laminar flow) is created. Each of these steps is somewhat arbitrary. Different detector functions, different amounts of smoothing, and different threshold levels can be chosen, and these must be based on the data. The implementation of Ching & LaGraff (1995) was used in the present work to find the leading and trailing edges of turbulent spots. However, this method cannot distinguish between the second-mode waves and turbulence.

Figure 21 shows the leading and trailing edges of the disturbances by marking them with dots at three different *Re*. The convection velocities can be calculated from the slope of the lines connecting these dots. Table 3 lists the convection velocities computed over all *Re*. The leading edge of the disturbances is readily

https://doi.org/10.1017/jfm.2014.475 Published online by Cambridge University Press

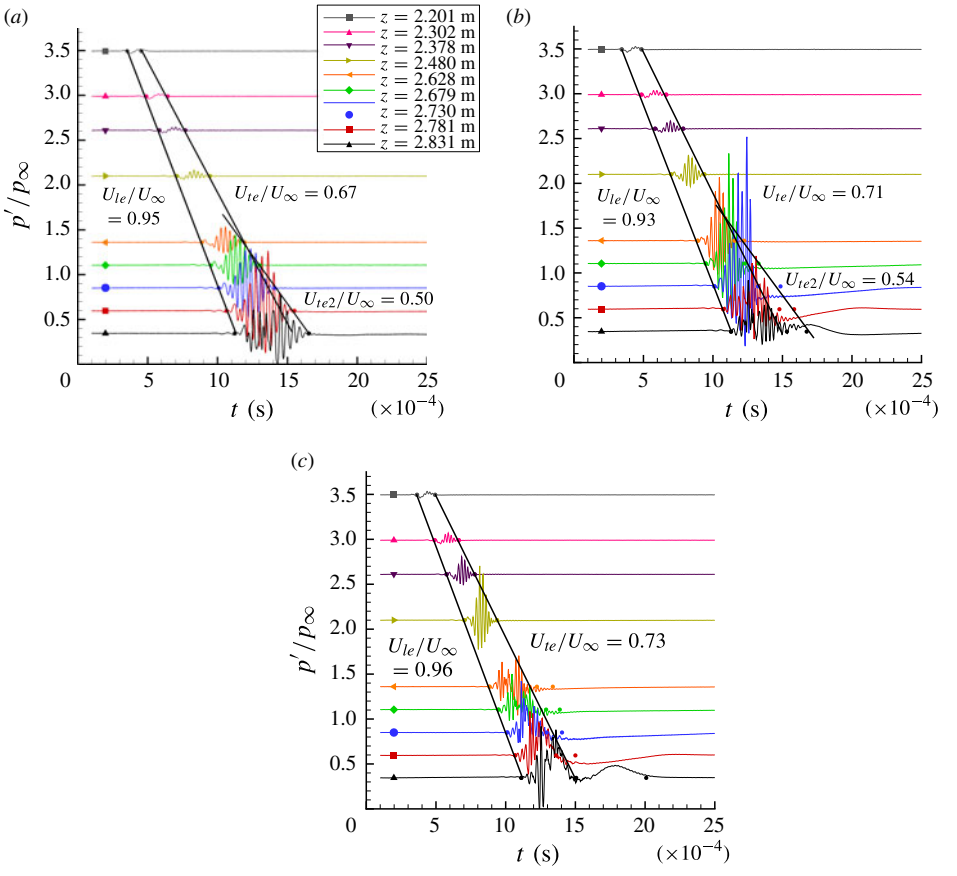


FIGURE 21. (Colour online) Convection velocities of controlled disturbances: (*a*) $Re = 6.33 \times 10^6$ m^{-1}; (*b*) $Re = 8.25 \times 10^6$ m^{-1}; (*c*) $Re = 10.8 \times 10^6$ m^{-1}.

distinguished and gives an average convection velocity of $0.95U_\infty$. The trailing edge is also distinguishable at the first four sensor locations. However, at higher *Re* when the waves break down to turbulent spots, there are additional second-mode fluctuations behind the disturbances. These fluctuations occur in the low-pressure calmed region behind the spots. Because they are out of phase, the ensemble averages barely show them. These smaller fluctuations were excluded from this estimate of the trailing-edge convection velocity (U_{te}/U_∞) by using a threshold three times as high to mark the trailing edge of the disturbances. The trailing-edge velocity increases with *Re* from $0.65U_\infty$ to $0.74U_\infty$. These velocities are in general agreement with DNS computations and experimental data (§ 1).

At low *Re*, the trailing-edge convection velocity of the disturbances seems to decrease to an average of $0.53U_\infty$ within the pipe insert (beginning at $z = 2.628$ m). At higher *Re*, if the additional second-mode fluctuations behind the disturbances are included, the trailing-edge convection velocity (U_{te2}/U_∞) is also decreased to an average of 0.52 U_∞. Above $Re = 8.85 \times 10^6$ m^{-1}, this change in convection velocity is not seen in the pipe insert, so estimates of this velocity are not included in table 3. It is unclear whether this change in convection velocity is an *Re* effect or due to the pipe insert.

https://doi.org/10.1017/jfm.2014.475 Published online by Cambridge University Press

$Re \times 10^6$ m^{-1}	U_{le}/U_∞	U_{te}/U_∞	U_{ave}/U_∞	U_{te2}/U_∞
5.80	0.94	0.64	0.79	0.55
6.33	0.95	0.67	0.81	0.50
7.00	0.97	0.69	0.83	0.46
7.57	0.94	0.70	0.82	0.54
8.25	0.93	0.71	0.82	0.54
8.85	0.95	0.73	0.84	0.53
9.53	0.95	0.74	0.85	—
10.2	0.95	0.74	0.84	—
10.8	0.96	0.73	0.84	—
Average	0.95	0.71	0.83	0.52

TABLE 3. Convection velocity of controlled disturbances at varying *Re*.

5.4.3. *Lateral spreading angle*

An estimate of the lateral spreading angle of the disturbances was computed using the method of Hedley & Keffer (1974). The front of the disturbances was picked at each spanwise location as before. A linear fit was made to these data to define the leading edge of the spot. This linear fit and the trailing-edge location defined in § 5.4.2 were used to compute the wing tip of the spots at $z = 2.679$, 2.730, and 2.781 m. The lateral spreading half-angle was then computed by the change in the spread of the disturbances with downstream distance. This was done at higher *Re* between 9.50 and 10.8×10^6 m^{-1} when the disturbances had begun to spread in the spanwise direction. Using this method, an average lateral spreading angle of $16 \pm 2°$ was found.

This spreading angle is very large compared to the expected lateral spreading half-angle of 2°–4° for Mach 6 (Fischer 1972). Fischer used oil flow or other low-frequency methods to define the spreading angle behind roughness elements for high-speed measurements. However, in other high-speed experiments, thin-film heat-transfer gauges were used (Mee 2002; Fiala *et al.* 2006). Fiala *et al.* (2006) found a spreading angle near 7° for edge Mach number $M_e = 3.5$ which is somewhat higher than Fischer's curve. Also, James (1958) found spreading angles up to almost 12° for $M_e = 3.9$ using schlieren images in orthogonal planes. These different techniques may not provide a consistent definition compared to the present high-frequency pressure data or Fischer's results.

Also, the present calculation included the second-mode waves in the determination of the spreading angle. James (1958) and Fiala *et al.* (2006) would not have had second-mode instabilities in their measurements because of the supersonic edge Mach numbers in their experiments. It may be that the second-mode disturbances in the current work propagate in the spanwise direction much more rapidly than the turbulent region in the core.

A second attempt to define the spanwise spreading angle without including the second-mode waves was done by using the 15 kHz low-pass filtered data shown in § 5.4.1. Three threshold levels of $0.05p'/p_\infty$, $0.08p'/p_\infty$, and $0.1p'/p_\infty$ were considered. For each z location, the point furthest from the centre was recorded and used to compute the spanwise spreading angle. An average spreading angle of $16 \pm 4°$ was found using the threshold level of $0.05p'/p_\infty$. The spanwise spreading angle was then re-computed for higher threshold levels. As the threshold level was increased from $0.05p'/p_\infty$ to $0.08p'/p_\infty$ to $0.1p'/p_\infty$, the spanwise spreading angle decreased from 16° to 12° to 8°. This smaller angle is more consistent with the results obtained

https://doi.org/10.1017/jfm.2014.475 Published online by Cambridge University Press

by James (1958) and Fiala *et al.* (2006). However, the dependence of the spreading angle on the threshold level shows the difficulties in using the pressure measurements to clearly define a spanwise spreading angle, especially since the instability waves and turbulence in the core of the disturbances cannot easily be separated.

6. Conclusions

The pressure fluctuations beneath turbulent spots and wavepackets were measured on the nozzle wall of the Boeing/AFOSR Mach-6 Quiet Tunnel. In contrast to the very thin boundary layers found on most wind-tunnel models, the thick laminar boundary layer on the nozzle wall of the BAM6QT allowed the study of turbulent spots at resolvable frequencies, with good spatial resolution, and without the contamination of acoustic noise found in conventional hypersonic tunnels.

Natural disturbances that break down into turbulent spots were studied on the nozzle wall. Two types of natural disturbances were found: large turbulent regions that develop near the throat and fill almost the entire nozzle circumference and smaller wavepackets with a later origin that break down into turbulent spots downstream. The intermittent turbulent regions were not studied as they were too large to exhibit typical spot characteristics. However, the smaller disturbances are characteristic of growth into turbulent spots. These initial wavepackets have frequencies in agreement with computations of second-mode waves on the nozzle wall. As the wavepackets grow larger, nonlinear harmonics are seen in power-spectral densities of the pressure fluctuations. Later, broadband frequencies develop in the spectra as the packets break down to turbulent spots. Spanwise measurements of the disturbances showed that typical wavepackets were ordered and narrow in extent. As the packets grew, they began to distort and spread in the spanwise direction. A low-pressure region also began to form behind larger packets. These packets then broke down into turbulent spots which had an arrowhead shape and a low-pressure ‘calmed’ region downstream, typical of low-speed turbulent spots. Instability wavepackets seemed to accompany these turbulent spots, especially at the leading edge of the disturbances. There was also evidence of instability waves in the ‘calmed’ region of some natural disturbances.

The natural disturbances show similar characteristics to controlled disturbances created by glow perturbations. Pulsed-glow perturbations, based on the electrical breakdown of air, were used to create repeatable perturbations at the unstable second-mode wave frequencies on the nozzle wall. This allowed a controlled study of the resulting wavepackets and turbulent spots; the origin of the disturbances could be established using the perturber, and repeat disturbances could be created and studied. Detailed centreline and spanwise measurements were made downstream of these controlled perturbations.

The pulsed-glow perturbations initially generate small instability wavepackets. The wave amplitudes grow with downstream distance and eventually become nonlinear, as indicated by the presence of harmonics in the spectra. The small wavepackets are narrow and ordered. As they become larger, they distort and spread in the spanwise direction. During the nonlinear growth, the waves can reach large amplitudes before breaking down to turbulence. A low-pressure ‘calmed’ region is seen developing behind the large wavepackets. Breakdown of the waves occurs first in the middle of the packet where the amplitude of the waves is largest. After breakdown, the central region of turbulence grows downstream and the typical arrowhead shape of the spots becomes evident, with a larger ‘calmed’ low-pressure region developing downstream. However, the second-mode waves remain an integral part of the disturbance; the waves

https://doi.org/10.1017/jfm.2014.475 Published online by Cambridge University Press

are still seen in the front and in the 'calmed' low-pressure region behind the spot as well as at the spanwise edges. As the spot progresses downstream, the turbulent portion of the spot grows larger in both the streamwise and spanwise directions. The second-mode waves are evident only at the periphery of the turbulence. Because of the gradual change from a wavepacket to a turbulent spot, the location where a packet becomes a spot is ambiguous. These measurements show a coexistence of second-mode instability waves with turbulent spots.

The present experiments are the first detailed measurements of the internal pressure structure of turbulent spots in a hypersonic boundary layer. They study the evolution of the pressure field in both instability wavepackets and turbulent spots. Spot growth parameters were computed from these measurements, and these results help validate DNS computations at high Mach numbers. Together, these measurements and complementary DNS studies can be used to develop better models of a hypersonic flight vehicle's environment.

Acknowledgements

This work could not have been completed without funding provided in part by the National Science Foundation Graduate Research Fellowship Program, Sandia National Laboratories, and AFOSR. Sandia National Laboratories is a multi-program laboratory managed and operated by Sandia Corporation, a wholly owned subsidiary of Lockheed Martin Corporation, for the US Department of Energy's National Nuclear Security Administration under contract DE-AC04-94AL85000. The Purdue School of Aeronautics and Astronautics machine shop built the experimental hardware used for this work. J. Phillips, the Purdue AAE department electronics technician, designed and built the perturber used for these measurements.

REFERENCES

BANE, S. P. M. 2010 Spark ignition: experimental and numerical investigation with application to aviation safety. PhD thesis, California Institute of Technology, Graduate Aerospace Laboratories.

BERESH, S. J., HENFLING, J. F., SPILLERS, R. W. & PRUETT, B. O. M. 2011 Fluctuating wall pressures measured beneath a supersonic turbulent boundary layer. *Phys. Fluids* **23**, 075110.

BERRIDGE, D. C. 2010 Measurements of second-mode instability waves in hypersonic boundary layers with a high-frequency pressure transducer. Master's thesis, Purdue University, School of Aeronautics & Astronautics.

CANTWELL, B., COLES, D. & DIMOTAKIS, P. 1978 Structure and entrainment in the plane of symmetry of a turbulent spot. *J. Fluid Mech.* **87**, 641–672.

CASPER, K. M. 2009 Hypersonic wind-tunnel measurements of boundary-layer pressure fluctuations. Master's thesis, Purdue University, School of Aeronautics & Astronautics.

CASPER, K. M. 2012 Pressure fluctuations beneath turbulent spots and instability wavepackets in a hypersonic boundary layer. PhD thesis, Purdue University School of Aeronautics & Astronautics.

CASPER, K. M., BERESH, S. J. & SCHNEIDER, S. P. 2011*a* Pressure fluctuations beneath turbulent spots and instability wavepackets in a hypersonic boundary layer. *AIAA Paper* 2011-372.

CASPER, K. M., BERESH, S. J. & SCHNEIDER, S. P. 2011*b* Spanwise growth of the turbulent spot pressure-fluctuation field in a hypersonic boundary layer. *AIAA Paper* 2011-3873.

CASPER, K. M., BERESH, S. J. & SCHNEIDER, S. P. 2012 Characterization of controlled perturbations in a hypersonic boundary layer. *AIAA Paper* 2012-281.

CHAMBERS, F. & THOMAS, A. 1983 Turbulent spots, wavepackets, and growth. *Phys. Fluids* **26** (5), 1160–1162.

CHING, C. Y. & LAGRAFF, J. E. 1995 Measurements of turbulent spot convection rates in a transitional boundary layer. *Exp. Therm. Fluid Sci.* **11**, 52–60.

https://doi.org/10.1017/jfm.2014.475 Published online by Cambridge University Press

CORRSIN, S. & KISTLER, A. L. 1955 Free-stream boundaries of turbulent flows. *NACA Tech. Rep.* 1244. (supersedes *NACA TN* 3133).

DENNIS, D. J. C. & NICKELS, T. B. 2008 On the limitations of Taylor's hypothesis in constructing long structures in a turbulent boundary layer. *J. Fluid Mech.* **614**, 197–206.

DHAWAN, S. & NARASIMHA, R. 1958 Some properties of boundary layer flow during the transition from laminar to turbulent motion. *J. Fluid Mech.* **3** (4), 418–435.

ESTORF, M., RADESPIEL, R., SCHNEIDER, S. P., JOHNSON, H. & HEIN, S. 2008 Surface-pressure measurements of second-mode instability in quiet hypersonic flow. *AIAA Paper* 2008-1153.

FIALA, A., HILLIER, R., MALLINSON, S. G. & WIJESINGHE, H. S. 2006 Heat transfer measurement of turbulent spots in a hypersonic blunt-body boundary layer. *J. Fluid Mech.* **555**, 81–111.

FISCHER, M. C. 1972 Spreading of a turbulent disturbance. *AIAA J.* **10** (7), 957–959.

FUJII, K. 2006 Experiment of two-dimensional roughness effect on hypersonic boundary-layer transition. *J. Spacecr. Rockets* **43** (4), 731–738.

GAD-EL HAK, M., BLACKWELDER, R. & RILEY, J. 1981 On the growth of turbulent regions in laminar boundary layers. *J. Fluid Mech.* **110**, 73–95.

GLEZER, A., KATZ, Y. & WYGNANSKI, I. 1989 On the breakdown of the wavepacket trailing a turbulent spot in a laminar boundary layer. *J. Fluid Mech.* **198**, 1–26.

GUTMARK, E. & BLACKWELDER, R. F. 1987 On the structure of a turbulent spot in a heated boundary layer. *Exp. Fluids* **5**, 217–229.

HAIDARI, A. & SMITH, D. 1994 The generation and regeneration of single hairpin vortices. *J. Fluid Mech.* **277**, 135–162.

HARRIS, J. E. & BLANCHARD, D. K. 1982 Computer program for solving laminar, transitional, or turbulent compressible boundary-layer equations for two-dimensional and axisymmetric flow. *NASA TM* 83207.

HEDLEY, T. B. & KEFFER, J. F. 1974 Turbulent/non-turbulent decisions in an intermittent flow. *J. Fluid Mech.* **64**, 625–644.

HOUBOLT, J. C. 1966 On the estimation of pressure fluctuations in boundary layers and wakes. *General Electric Report* TIS 66SD296.

JAMES, C. S. 1958 Observations of turbulent-burst geometry and growth in supersonic flow. *NACA TN* 4235.

JOHANSSON, A., HER, J. & HARITONIDUS, J. 1987 On the generation of high-amplitude wall-pressure peaks in turbulent boundary layers and spots. *J. Fluid Mech.* **175**, 119–142.

JOHNSON, C. B., STAINBACK, P. C., WICKER, K. C. & BONEY, L. R. 1972 Boundary-layer edge conditions and transition Reynolds number data for a flight test at Mach 20 (Reentry F). *NASA TM* X-2584.

JOKSCH, A. & KLEISER, L. 2008 Growth of turbulent spots in high-speed boundary layers on a flat plate. *Intl J. Heat Fluid Flow* **29**, 1543–1557.

JULIANO, T., SEGURA, R., BORG, M., CASPER, K., HANNON, M., WHEATON, B. & SCHNEIDER, S. 2008 Starting issues and forward-facing cavity resonance in a hypersonic quiet tunnel. *AIAA Paper* 2008-3735.

KATZ, Y., SEIFERT, A. & WYGNANSKI, I. 1990 On the evolution of the turbulent spot in a laminar boundary layer with a favourable pressure gradient. *J. Fluid Mech.* **221**, 1–22.

KEYES, F. G. 1951 A summary of viscosity and heat-conduction data for He, A, H_2, O_2, N_2, CO, CO_2, H_2O, and air. *Trans. ASME* **73**, 589–596.

KIMMEL, R. L., DEMETRIADES, A. & DONALDSON, J. 1995 Space–time correlation measurements in a hypersonic transitional boundary layer. *AIAA Paper* 95-2292.

KIMMEL, R. L. & KENDALL, J. M. 1991 Nonlinear disturbances in a hypersonic laminar boundary layer. *AIAA Paper* 1991-0320.

KRISHNAN, L. & SANDHAM, N. D. 2006*a* Effect of Mach number on the structure of turbulent spots. *J. Fluid Mech.* **566**, 225–234.

KRISHNAN, L. & SANDHAM, N. D. 2006*b* On the merging of turbulent spots in a supersonic boundary layer flow. *Intl J. Heat Fluid Flow* **27**, 542–550.

LADOON, D. W. 1998 Wavepackets generated by a surface glow discharge on a cone at Mach 4. PhD thesis, Purdue University, School of Aeronautics & Astronautics.

https://doi.org/10.1017/jfm.2014.475 Published online by Cambridge University Press

LAGRAFF, J. E. & JONES, T. V. 1995 Turbulent spot growth rates and generation in a compressible boundary layer. *AFOSR TR* 96-0070 (citation ADA304396 in DTIC).

MACK, L. M. 1984 Boundary layer linear stability theory. In *Report 709, Special Course on Stability and Transition of Laminar Flow*, pp. 1–81. AGARD.

MAKITA, H. & NISHIZAWA, A. 2001 Characteristics of internal vortical structures in a merged turbulent spot. *J. Turbul.* **2** (12), 1–14.

MAUTNER, T. S. 1983 Investigation of the wall pressure, wall shear stress and velocity fields associated with a turbulent spot in a laminar boundary layer. PhD thesis, University of California, San Diego.

MAUTNER, T. S. 1988 Comparison of the wall pressure fluctuations in artificially generated turbulent spots, natural transition and turbulent boundary layers. *AIAA Paper* 1988-0409.

MAUTNER, T. S. & VAN ATTA, C. W. 1982 An experimental study of the wall-pressure field associated with a turbulent spot in a laminar boundary layer. *J. Fluid Mech.* **118**, 59–77.

MEE, D. J. 2002 Boundary-layer transition measurements in hypervelocity flows in a shock tunnel. *AIAA J.* **40** (8), 1542–1548.

MEE, D. J. & GOYNE, C. P. 1996 Turbulent spots in boundary layers in a free-piston shock-tunnel flow. In *Shock Waves*, vol. 6, pp. 337–343. Springer.

NARASIMHA, R. 1985 The laminar-turbulent transition zone in the boundary layer. *Prog. Aerosp. Sci.* **22**, 29–80.

PARK, S. & LAUCHLE, G. 2009 Wall pressure fluctuation spectra due to boundary-layer transition. *J. Sound Vib.* **319**, 1067–1082.

PATE, S. R. & BROWN, M. D. 1969 Acoustic measurements in supersonic transitional boundary layers. *AEDC TR* 69-182.

RAMAN, K. R. 1974 A study of surface pressure fluctuations in hypersonic turbulent boundary layers. *NASA Contractor Rep.* 2386.

REDFORD, J. A., SANDHAM, N. D. & ROBERTS, G. T. 2012 Numerical simulations of turbulent spots in supersonic boundary layers: effects of Mach number and wall temperature. *Prog. Aerosp. Sci.* **52**, 67–79.

RILEY, J. J. & GAD-EL HAK, M. 1984 The dynamics of turbulent spots. In *Frontiers in Fluid Mechanics* (ed. S. H. Davis & J. L. Lumley), pp. 123–155. Springer.

SANKARAN, R. & ANTONIA, R. A. 1988 Influence of a favorable pressure gradient on the growth of a turbulent spot. *AIAA J.* **26** (7), 885–887.

SANKARAN, R., SOKOLOV, M. & ANTONIA, R. 1988 Substructures in a turbulent spot. *J. Fluid Mech.* **197**, 389–414.

SAVAS, O. 1979 Some measurements in synthetic turbulent boundary layers. PhD thesis, California Institute of Technology, Graduate Aeronautical Laboratories.

SCHNEIDER, S. P. 1998 Design of a Mach-6 quiet-flow wind-tunnel nozzle using the e**N method for transition estimation. *AIAA Paper* 98-0547.

SCHNEIDER, S. 2000 Laminar-flow design for a Mach-6 quiet-flow wind tunnel nozzle. *Curr. Sci.* **79** (6), 790–799.

SCHNEIDER, S. P. 2008 The development of hypersonic quiet tunnels. *J. Spacecr. Rockets* **45** (4), 641–664.

SCHUBAUER, G. B. & KLEBANOFF, P. S. 1955 Contributions on the mechanics of boundary-layer transition. *NACA Rep.* 1289.

SEIFERT, A. & WYGNANSKI, I. 1995 On turbulent spots in a laminar boundary layer subjected to a self-similar adverse pressure gradient. *J. Fluid Mech.* **296**, 185–209.

SEIFERT, A., ZILBERMAN, M. & WYGNANSKI, I. 1994 On the simultaneous measurements of two velocity components in the turbulent spot. *J. Engng Maths* **28**, 43–54.

SINGER, B. 1996 Characteristics of a young turbulent spot. *Phys. Fluids* **8** (2), 509–521.

SIVASUBRAMANIAN, J. & FASEL, H. F. 2010*a* Direct numerical simulation of a turbulent spot in a cone boundary layer at Mach 6. *AIAA Paper* 2010-4599.

SIVASUBRAMANIAN, J. & FASEL, H. F. 2010*b* Numerical investigation of boundary-layer transition initiated by a wavepacket for a cone at Mach 6. *AIAA Paper* 2010-900.

https://doi.org/10.1017/jfm.2014.475 Published online by Cambridge University Press

SIVASUBRAMANIAN, J. & FASEL, H. F. 2011 Transition initiated by a localized disturbance in a hypersonic flat-plate boundary layer. *AIAA Paper* 2011-374.

STEEN, L. E. 2010 Characterization and development of nozzles for a hypersonic quiet wind tunnel. Master's thesis, Purdue University, School of Aeronautics & Astronautics.

TAYLOR, G. I. 1938 The spectrum of turbulence. *Proc. R. Soc. Lond.* A **164**, 476–490.

VINOD, N. 2007 The signature of laminar instabilities in the zone of transition to turbulence. *J. Turbul.* **8** (2).

WADHAMS, T. P., MUNDY, E., MACLEAN, M. G. & HOLDEN, M. S. 2008 Ground test studies of the HIFIRE-1 transition experiment part 1: experimental results. *J. Spacecr. Rockets* **45** (6), 1134–1148.

WHEATON, B. 2009 Roughness-induced instability in a laminar boundary layer at Mach 6. Master's thesis, Purdue University, School of Aeronautics & Astronautics.

WYGNANSKI, I., SOKOLOV, M. & FRIEDMAN, D. 1976 On a turbulent 'spot' in a laminar boundary layer. *J. Fluid Mech.* **78**, 785–819.

WYGNANSKI, I., ZILBERMAN, M. & HARITONIDIS, J. 1982 On the spreading of a turbulent spot in the absence of a pressure gradient. *J. Fluid Mech.* **123**, 69–90.

ZANCHETTA, M. 1996 Kinetic heating and transition studies at hypersonic speeds. PhD thesis, Imperial College of Science, Technology, and Medicine.

ZHAROV, V. A., HTUN, H. & KHLOPKOV, Y. I. 2009 Statistical modeling of the turbulent transition in the boundary layer. *J. Appl. Mech. Tech. Phys.* **50** (5), 742–746.

ZILBERMAN, M., WYGNANSKI, I. & KAPLAN, R. E. 1977 Transitional boundary layer spot in a fully turbulent environment. *Phys. Fluids* **20**, S258–S271.

https://doi.org/10.1017/jfm.2014.475 Published online by Cambridge University Press